ISSN 1590-8844
Vol. 11 No 02
2010

International Journal of Mechanics and Control

Editor: Andrea Manuello Bertetto

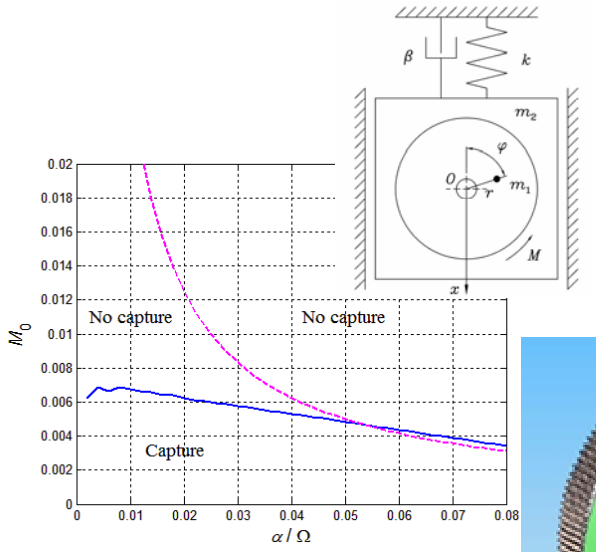

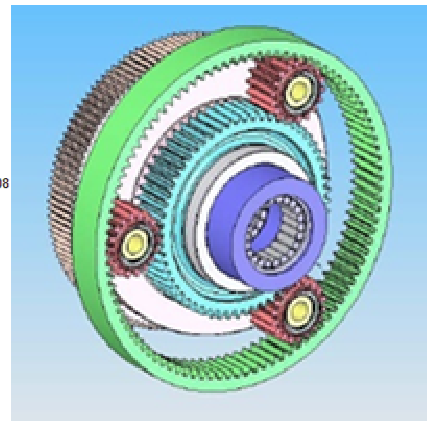

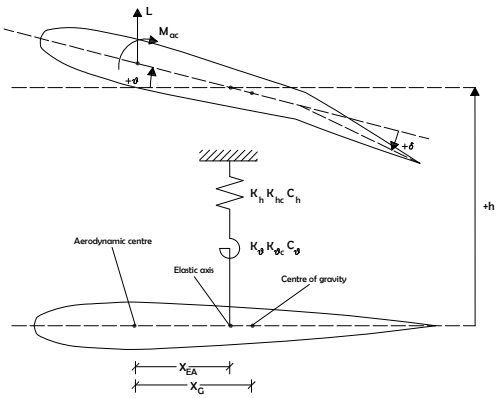

LIBRERIA EDITRICE UNIVERSITARIA
LEVROTTO & BELLA
TORINO

Official Torino Italy Court Registration
n.5390, 5th May 2000

Deposito presso il Tribunale di Torino
numero 5390 del 5 maggio 2000
Direttore responsabile:
Andrea Manuello Bertetto

International Journal of Mechanics and Control

The Journal is addressed to scientists and engineers who work in the fields of mechanics (mechanics, machines, systems, control, structures). It is edited in Turin (Northern Italy) by Levrotto&Bella Co., with an international board of editors. It will have not advertising.

Turin has a great and long tradition in mechanics and automation of mechanical systems. The journal would will to satisfy the needs of young research workers of having their work published on a qualified paper in a short time, and of the public need to read the results of researches as fast as possible.

Interested parties will be University Departments, Private or Public Research Centres, Innovative Industries.

Aims and scope

The *International Journal of Mechanics and Control* publishes as rapidly as possible manuscripts of high standards. It aims at providing a fast means of exchange of ideas among workers in Mechanics, at offering an effective method of bringing new results quickly to the public and at establishing an informal vehicle for the discussion of ideas that may still in the formative stages.

Language: English

International Journal of Mechanics and Control will publish both scientific and applied contributions. The scope of the journal includes theoretical and computational methods, their applications and experimental procedures used to validate the theoretical foundations. The research reported in the journal will address the issues of new formulations, solution, algorithms, computational efficiency, analytical and computational kinematics synthesis, system dynamics, structures, flexibility effects, control, optimisation, real-time simulation, reliability and durability. Fields such as vehicle dynamics, aerospace technology, robotics and mechatronics, machine dynamics, crashworthiness, biomechanics, computer graphics, or system identification are also covered by the journal.

Please address contributions to

Prof. Guido Belforte
Prof. Andrea Manuello Bertetto
PhD Eng. Elvio Bonisoli

Dept. of Mechanics
Technical University - Politecnico di Torino
C.so Duca degli Abruzzi, 24.
10129 - Torino - Italy - E.C.

www.jomac.it
e_mail: jomac@polito.it

Subscription information

Subscription order must be sent to
the publisher:

Libreria Editrice Universitaria
Levrotto&Bella
2/E via Pigafetta – 10129 Torino – Italy

www.levrotto-bella.net
e_mail: info@levrotto-bella.net
tel. +39.011.5097367
+39.011.5083690
fax +39.011.504025

ISSN 1590-8844
International Journal of Mechanics and Control, Vol. 11, No. 02, 2010

DETERMINATION OF A CRITERION TO PREDICT THE RESONANCE CAPTURE OF AN UNBALANCED ROTOR

E. Bonisoli* F. Vatta** A. Vigliani**

* Dipartimento di Sistemi di Produzione - Politecnico di Torino - C.so Duca degli Abruzzi, 24 - 10129 Torino - ITALY

** Dipartimento di Meccanica - Politecnico di Torino - C.so Duca degli Abruzzi, 24 - 10129 Torino - ITALY

ABSTRACT

The paper presents the analysis of the transient behaviour of a rotor-disk system in the neighbourhood of the critical speed. In such conditions, the rotor may be captured in resonance, thus being unable to increase its angular speed.
The aim of the study is to determine a criterion suitable to predict the system behaviour for different values of external torque and bearings damping.

Keywords: rotordynamics, resonance capture

1 INTRODUCTION

The dynamic behaviour of unbalanced rotors mounted on elastic bearings represents an interesting engineering problem since, during the transient motion, when the system goes through the rotor critical velocity field, complex dynamical phenomena can occur ([1]). In fact, even in presence of small unbalances, during the rotor angular speed transients the system can be captured in resonance ([1,2]); this capture occurs when the energy, supplied to the system by means of an external torque in order to accelerate the angular velocity, indeed causes the growth of translational oscillations. Under such conditions, the rotor angular speed oscillates around a value correspondent to the translational critical frequency of the system, without being able to cross this value ([3]).
The conditions, which favour the possible lock of the system in resonance, are mainly associated to limited values of the external torque and of the damping of the bearings. In the case of resonance capture, the damping is insufficient to dissipate the energy introduced in the system by the external torque; hence the translational motion grows at the expense of the angular speed, which maintains an almost constant value.

Contact author: E. Bonisoli[1], F. Vatta[2], A. Vigliani[3]

[1] elvio.bonisoli@polito.it
[2] furio.vatta@polito.it
[3] alessandro.vigliani@polito.it

The paper aims to investigate the aforementioned phenomenon with approximate analytical and numerical techniques, in order to foresee the capture conditions without using the differential formulations present in the literature ([3]). Hence the authors present a two degrees of freedom nonlinear model able to describe the capture phenomenon and consequently to analyse the system behaviour with almost-stationary techniques, for different values of damping and external power. The goal is to define a criterion that will allow to foresee the capture conditions without the need of numerical integration of the equations of motion.
The analytical and numerical analysis presented in the paper allows to draw the following conclusions with regard to the resonance capture:

- it occurs only in proximity of the translational critical frequency;
- for low damped systems, it may arise for external torques quite smaller than those predicted with a almost–stationary approach, while for highly damped rotors the different approaches give nearly the same results.

The method developed in the paper proves a useful tool in predicting the system transient behaviour and it can be successfully applied during the system design, since it allows to evaluate the minimum torque value necessary to avoid resonance capture.

2 ROTOR MODEL

Similarly to the model proposed by Dimentberg & al. ([3]), the authors consider a vertical rotor mounted on elastic bearings; the shaft is described as a rigid body. Figure 1 illustrates the system configuration at a general time.

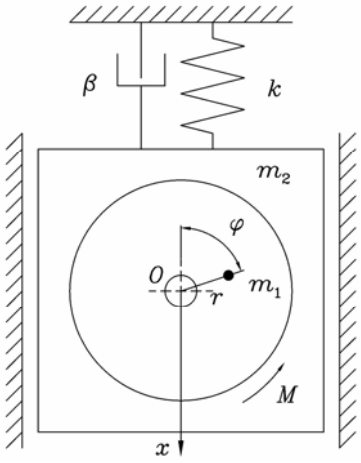

Figure 1 Two d.o.f. rotor model.

Under the hypothesis that the axial symmetric rotor can translate only along x direction, the system nonlinear dynamic equations are:

$$\begin{aligned} &m_t\ddot{x}+\beta\dot{x}+kx=m_1 r(\dot{\phi}^2\cos\phi+\ddot{\phi}\sin\phi)\\ &I\ddot{\phi}=M+m_1 r\ddot{x}\sin\phi \end{aligned} \tag{1}$$

where $I=J+m_1 r^2$ and $m_t=m_1+m_2$, being m_1 the disk mass, m_2 the mass of shaft and bearings, J the disk inertia, r the disk eccentricity, k and β the bearings stiffness and damping respectively, M the external torque, x and ϕ the system translational and rotational degrees of freedom.
Let

$$\begin{aligned} &\alpha=\frac{\beta}{2m_t} \quad \Omega^2=\frac{k}{m_t} \quad M_0\left(1-\varepsilon\dot{\phi}\right)=\frac{M}{I}\\ &q_1=\frac{m_1}{m_t}r \quad q_2=\frac{m_1}{I}r \quad q=q_1 q_2 \end{aligned} \tag{2}$$

where ε is the torque constant of the engine; then equations (1) become:

$$\begin{aligned} &\ddot{x}+2\alpha\dot{x}+\Omega^2 x=q_1(\dot{\phi}^2\cos\phi+\ddot{\phi}\sin\phi)\\ &\ddot{\phi}=M_0(1-\varepsilon\dot{\phi})+q_2\ddot{x}\sin\phi \end{aligned} \tag{3}$$

Finally, let

$$\bar{x}=\frac{x}{q_1} \text{ and } \tau=\Omega t; \tag{4}$$

consequently

$$\begin{aligned} &\frac{d}{dt}(\cdot)=\Omega\frac{d}{d\tau}(\cdot)=\Omega(\cdot)'\\ &\frac{d^2}{dt^2}(\cdot)=\Omega^2\frac{d^2}{d\tau^2}(\cdot)=\Omega^2(\cdot)'' \end{aligned} \tag{5}$$

The system can now be written in non-dimensional form:

$$\begin{aligned} &\bar{x}''=-\frac{2\alpha}{\Omega}\bar{x}'-\bar{x}+\phi'^2\cos\phi+\phi''\sin\phi\\ &\phi''=\frac{M_0}{\Omega^2}(1-\varepsilon\Omega\phi')+\bar{x}'\sin\phi \end{aligned} \tag{6}$$

Equations (6) will be analysed under the hypotheses of null initial conditions and external torque independent of the angular speed (i.e. $\varepsilon=0$); consequently the rotor dynamics strongly depends on the external torque M_0 and on damping α which represents the only dissipative term of the system.
Some examples of numerical integration of equations (6), showing both capture/no capture time histories, are presented in Fig. 2÷4 ($q=0.001$, $\varepsilon=0$); the numerical analysis allows to clarify some aspects of the dynamic behaviour, as described in what follows. For small external torques ($\alpha/\Omega=0.01$, $M_0/\Omega^2=0.0065$), the system angular speed grows almost linearly (Fig. 2-right) up to the system natural frequency $\omega=\Omega$, when the rotor translational motion cannot be neglected (Fig. 2-left). The nonlinear coupling of the second equation of (6) forces the mean value of the angular acceleration to decrease (Fig. 4), thus leading the angular speed towards capture, as shown in the following section. For larger values of the torque ($\alpha/\Omega=0.01$, $M_0/\Omega^2=0.008$), the rotor angular speed still grows linearly (Fig. 3-right), but when approaching the natural frequency $\omega=\Omega$ it remains in such condition for a short time. The nonlinear coupling term of the second equation of (6) provokes a small decrease of the angular acceleration, that, after a transient, returns to a mean value close to the one shown in the initial region of Fig. 4 (right): in this situation the resonance capture does not take place, as it may be seen also in Fig. 3.
Observing the different dynamic behaviour, it appears that the sign change of the mean value of the angular acceleration (dash-dotted line in Fig. 4) can be considered an indicative parameter of the capture condition; in particular, considering the mean acceleration, it can be observed that if its first oscillation shows negative values, the system will evolve towards capture.

3 APPROXIMATE ANALYSIS

3.1 LINEARIZATION OF THE TRANSLATIONAL EQUATION

When the resonance capture takes place (e.g. $\alpha/\Omega=0.01$, $M_0/\Omega^2=0.0065$) the rotor almost stationary condition can be represented by the mean values of the translational oscillations and of the angular speed respectively (Fig. 2). Consequently, the rotor angular acceleration (obtained by numerical integration of eq.(6) and whose mean value is plotted in solid line in Fig. 4) oscillates around the null value.

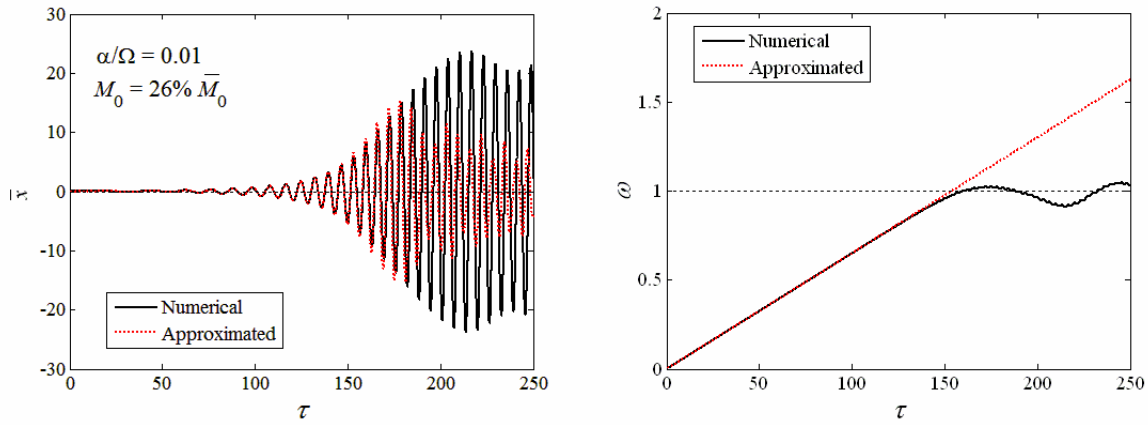

Figure 2 Exact and approximate solution in capture conditions: $\bar{x}$ vs. τ (left) and ω vs. τ (right).

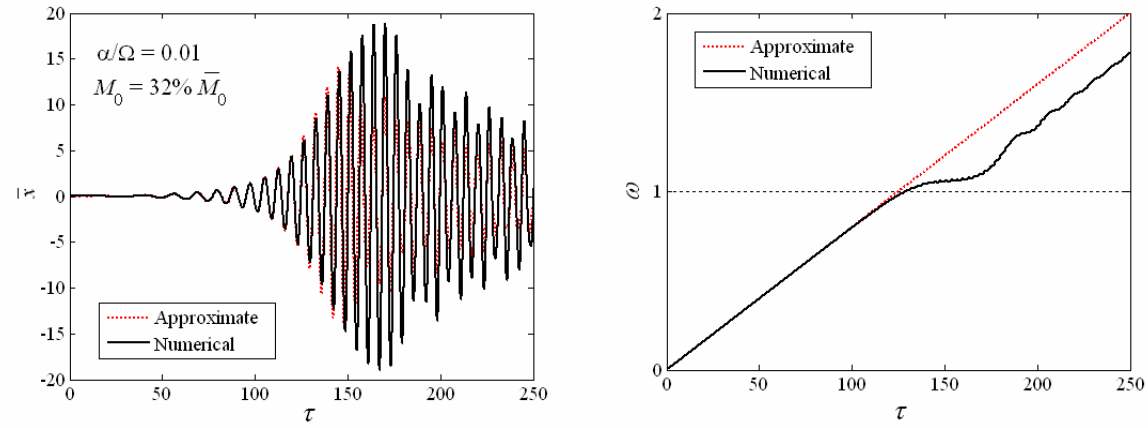

Figure 3 Exact and approximate results for non-capture case: $\bar{x}$ vs. . τ (left) and ω vs. τ (right).

Adopting an approximate technique, let consider $\phi' \approx \text{const}$; obviously $\phi'' \approx 0$ and hence, being $\varphi' = \bar{\omega}\tau$, where $\bar{\omega} = \omega/\Omega$, the first of eq. (6) becomes:

$$\bar{x}'' + \frac{2\alpha}{\Omega}\bar{x}' + \bar{x} = \bar{\omega}^2 \cos\bar{\omega}\tau \tag{7}$$

whose particular solution can be sought in the form $\bar{x}_P = \bar{x}_0 \cos(\bar{\omega}\tau + \psi)$, with $\bar{x}_0$ real and positive. The translational oscillation modulus and phase are:

$$\bar{x}_0 = \frac{\bar{\omega}^2}{\sqrt{(1-\bar{\omega}^2)^2 + 4\alpha^2\bar{\omega}^2/\Omega^2}}$$
$$\psi = \arctan\frac{-2\alpha\bar{\omega}/\Omega}{1-\bar{\omega}^2} \tag{8}$$

Substituting such solution in the second of eq. (6), it yields:

$$\phi'' = \frac{M_0}{\Omega^2}(1-\varepsilon\Omega\phi') - q\bar{x}_0\bar{\omega}^2\cos(\bar{\omega}\tau+\psi)\sin(\bar{\omega}\tau) \tag{9}$$

considering the mean value, it holds:

$$\phi'' = \frac{M_0}{\Omega^2}(1-\varepsilon\Omega\phi') - \frac{q\alpha\bar{\omega}^5/\Omega}{(1-\bar{\omega}^2)^2 + 4\alpha^2\bar{\omega}^2/\Omega^2} \tag{10}$$

Now, let $\phi'' \approx 0$; hence

$$\frac{M_0}{\Omega^2}(1-\varepsilon\Omega\phi') = \frac{q\alpha\bar{\omega}^5/\Omega}{(1-\bar{\omega}^2)^2 + 4\alpha^2\bar{\omega}^2/\Omega^2} \tag{11}$$

then the capture condition $\bar{\omega} = 1$ (i.e. $\omega = \Omega$) allows to determine the torque "limit" value:

$$\bar{M}_0 = M_0(1-\varepsilon\Omega\phi') = \frac{q\Omega^3}{4\alpha} \tag{12}$$

It must be underlined that Dimentberg & al. ([3]) determine the same torque "limit" value by means of an asymptotic method that approximates the system behaviour over a period; to estimate the capture / no capture condition, these Authors use a numerical procedure consisting in progressive decrements of the "limit" value itself. It is worth noting that, as a matter of fact, the "real" value of the torque required to cross the capture region is only a percentage of the "limit" value and it strongly depends on the system damping (Fig. 6); moreover also the system initial conditions influence the capture condition ([2]).

If the external torque is smaller than the "limit" value $\bar{M}_0$ of eq. (12), as in the example of Fig. 2 and 4 (where $M_0 = 26\%\,\bar{M}_0$), then eq. (11) is a fifth-degree equation in $\bar{\omega} = \omega/\Omega$, having three real and two complex conjugate solutions; the three real values, as it can be proved numerically, represent in increasing order the resonance capture speed (stable equilibrium), an unstable equilibrium velocity and the asymptotic speed of the rotor in case it passes through the capture condition ([3]).

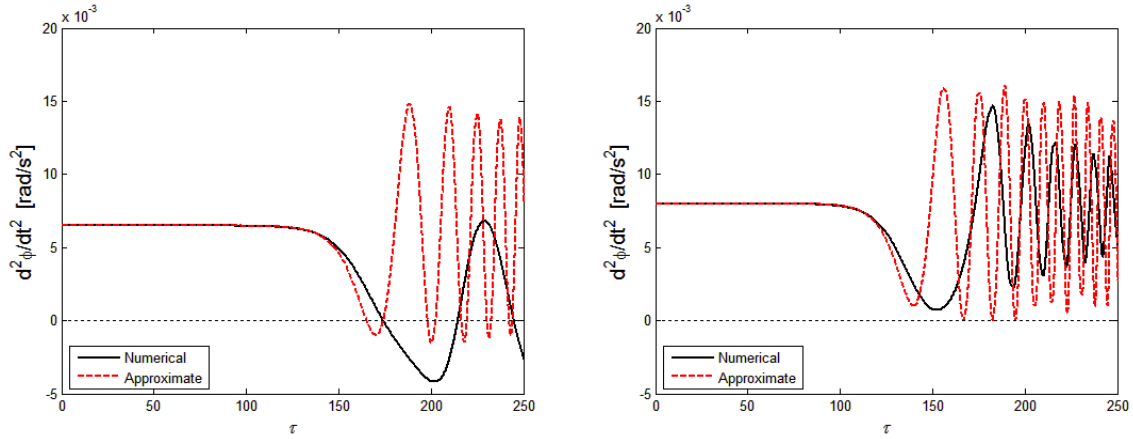

Figure 4 Exact and approximate mean values of the angular acceleration: capture (left: $M_0 = 26\%\,\overline{M}_0$) and non-capture (right: $M_0 = 32\%\,\overline{M}_0$).

Unfortunately, the analysis of the stationary condition does not lead to a significant index to discriminate the capture condition since eq. (11) and eq. (12) do not describe the system dynamic behaviour in transient motion; therefore $\overline{M}_0$ does not correspond to the effective threshold. Hence, as previously stated, in order to determine an effective criterion for capture, the transient analysis appears fundamental.

3.2 LINEARIZATION OF THE ROTATIONAL EQUATION

When the rotor is not captured (e.g. $\alpha/\Omega = 0.01$, $M_0 = 32\%\,\overline{M}_0$), the dynamic condition may be represented by a linear increase for the rotor angular velocity (Fig. 3-right) and by a frequency sweep with constant acceleration for the translational oscillations (Fig. 3 - left).

Consequently, the angular acceleration tends to possess a constant mean value, perturbed in the neighbourhood of the translational resonance frequency crossing (Fig. 3-right and 4).

Under the assumption that, for velocities smaller than the critical speed (i.e. $\varphi' = \overline{\omega} \le 1$), the nonlinear term can be neglected (i.e. $\bar{x}''\sin\phi \approx 0$), from the second of eq. (6) it holds:

$$\phi'' = \frac{M_0}{\Omega^2} - \frac{\varepsilon M_0 \phi'}{\Omega}, \tag{13}$$

whose solution is given by the sum of the particular solution $\varphi'_P = 1/(\varepsilon\Omega) =$ constant plus the homogeneous solution $\varphi'_H = A\,e^{-M_0\tau/\Omega}$. If the initial conditions are $\varphi'(\tau = 0) = \varphi'_0$, it holds:

$$\varphi'(\tau) = \varphi'_0\, e^{-M_0\tau/\Omega} + \frac{1 - e^{-M_0\tau/\Omega}}{\varepsilon\Omega}. \tag{14}$$

Let the external torque be constant (i.e. $\varepsilon = 0$); then:

$$\phi'' = \frac{M_0}{\Omega^2}, \tag{15}$$

whose solution is simply

$$\varphi'(\tau) = \varphi'_0 + \frac{M_0}{\Omega^2}\tau; \tag{16}$$

hence the final value of τ for which $\overline{\omega} = \Omega$ is

$$\tau = \frac{(1 - \varphi'_0)\Omega^2}{M_0}. \tag{17}$$

Substituting this solution in the first of eq. (6), it yields:

$$\bar{x}'' + \frac{2\alpha}{\Omega}\bar{x}' + \bar{x} = \left(\varphi'_0 + \frac{M_0}{\Omega^2}\tau\right)^2 \cos\left(\varphi_0 + \varphi'_0\tau + \frac{M_0}{2\Omega^2}\tau^2\right) + \frac{M_0}{\Omega^2}\sin\phi\left(\varphi_0 + \varphi'_0\tau + \frac{M_0}{2\Omega^2}\tau^2\right) \tag{18}$$

that can be expressed in the form

$$\bar{x}'' + \frac{2\alpha}{\Omega}\bar{x}' + \bar{x} = C\sin(\vartheta + \Theta), \tag{19}$$

where

$$C = \sqrt{\left(\varphi'_0 + \frac{M_0}{\Omega^2}\tau\right)^4 + \frac{{M_0}^2}{\Omega^4}}$$

$$\vartheta = \varphi_0 + \varphi'_0\tau + \frac{M_0}{2\Omega^2}\tau^2 \tag{20}$$

$$\Theta = \arctan\frac{\left(\varphi'_0 + \frac{M_0}{\Omega^2}\tau\right)^2}{\frac{M_0}{\Omega^2}}$$

The solution $\bar{x}(\tau)$ can be seen as the convolution of two functions correspondent to the linear system impulse response $h(\tau)$ and to a generic force $f(\tau)$, i.e.:

$$\bar{x}(\tau) = h(\tau) * f(\tau), \tag{21}$$

or

$$\bar{x}(\tau) = \Im^{-1}[H(\omega)\cdot F(\omega)], \tag{22}$$

where $H(\omega)$ and $F(\omega)$ are the Fourier transforms of $h(\tau)$ and $f(\tau)$.

In particular, assuming that the constant terms can be neglected, the generic force $f(\tau)$ represents a frequency

sweep with constant acceleration (i.e. $C \propto \tau^2$); consequently, if the angular speed is increased slowly, the almost-stationary translational response of eq.(19) would show approximately the amplitude expressed in eq.(8).

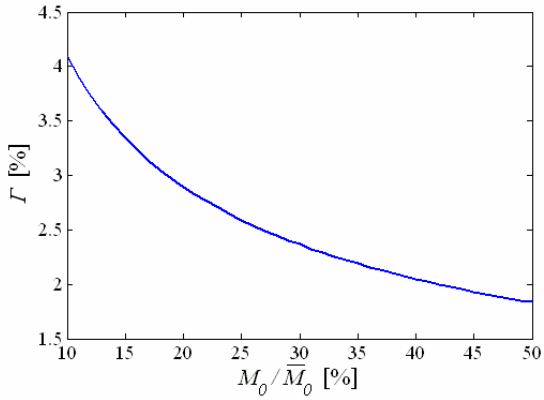

Figure 5 Coefficient Γ.

In Fig. 2÷4 the numerical response (solid line) is compared to the approximate solution (dashed line) given in eq.(22). It is possible to state that the approximate model can accurately describe the system dynamical behaviour for angular speed $\overline{\omega} \le 1$, both in case of capture and escape: in particular, the first oscillation of the mean value of angular acceleration towards negative values is sufficiently represented, though in advance.

4 TRANSIENT ANALYSIS

The analysis of the time solutions of nonlinear eq.(6) plotted in Fig. 4 underlines that the sign change of the acceleration mean value can be considered a parameter strictly connected to the dynamical bifurcation of the system. Hence it proves an efficient index to foresee the capture condition.

These considerations lead to the research of an analytical expression, which will allow foreseeing the capture conditions without having to solve numerically the equation of motion.

In order to approximate the mean angular acceleration ϕ'', i.e. the second expression in eq.(6), the following expression is suggested:

$$\phi'' = \frac{M_0}{\Omega^2}(1 - \varepsilon\Omega\phi') + \\ - q\Gamma\Omega^2 u\left(\tau - \frac{\Omega^2}{M_0}\right) e^{-\frac{1}{2}\frac{\alpha}{\Omega}\left(\tau - \frac{\Omega^2}{M_0}\right)} \sin\left[\frac{M_0}{2\Omega^2}\left(\tau - \frac{\Omega^2}{M_0}\right)^2\right] \quad (23)$$

where, according to the approximate expression of the translational response given in eq. (22), the mean angular acceleration ϕ'' is described by two terms: the first one corresponds to the value given in (13), while the second term describes the fundamental harmonic of the oscillations that are responsible for the bifurcation in the neighbourhood of the translational resonance.

The non-dimensional coefficient Γ in eq. (23) depends on $M_0/\overline{M}_0$ and corresponds to the ratio between the amplitude of the displacement $\bar{x}$ obtained solving eq. (18) and the displacement in almost-stationary conditions computed in eq. (8). Hence it can be seen that eq. (18) corresponds to eq. (7), while $u(\tau - \Omega^2/M_0)$ is the step function at $\tau = \Omega^2/M_0$, with null initial conditions.

Figure 5 plots coefficient Γ versus the external torque $M_0/\overline{M}_0$; this plot is built through the estimate of the Fourier transform modulus of the force acting on the translational system (eq. 19) divided by the corresponding squared angular speed.

For an almost-harmonic force with linearly variable frequency and with amplitude dependent on the squared frequency, coefficient Γ can be interpreted as the weight of the external force in exciting the translational stationary response. Hence, the second term of eq. (23) represents the mean perturbation of the angular acceleration due to the translational system response to a frequency sweep with constant acceleration; consequently, it can be represented with a negative exponential term proportional to α and by a periodic term shifted in time and whose frequency depends on time squared.

In consequence of the proposed approximations, Fig. 6 (left) plots the capture discriminant function against damping α: the dot-dashed line is the numerical integration, the dashed one is the solution deter- mined through the first intersection of the angular acceleration with the zero axis, while the solid line is the empirical expression shown in eq.(23). It is evident that, for given values of the external torque, the capture regions strongly depend on damping. The right side of Fig. 6 shows the comparison with the results obtained in eq. (12) through the linearization of the translational equation: it appears that also for low damping, the torque required to pass through the resonance frequency is finite, while the value predicted in eq. (12) tends to infinite. Hence, the proposed approximate analysis leads to the empirical solution (eq. 23) that represents an effective approach to describe the transition of the dynamical behaviour: in fact, if a sign change in (eq. 23) occurs, then the system is captured in resonance.

5 CONCLUSIONS

The nonlinear dynamical behaviour of a two d.o.f. rotor is investigated with approximate techniques; in particular, the bifurcation phenomenon known as “resonance capture” is modelled to permit an estimation of the dynamic behaviour of the system, without using the differential formulation proposed in the literature.

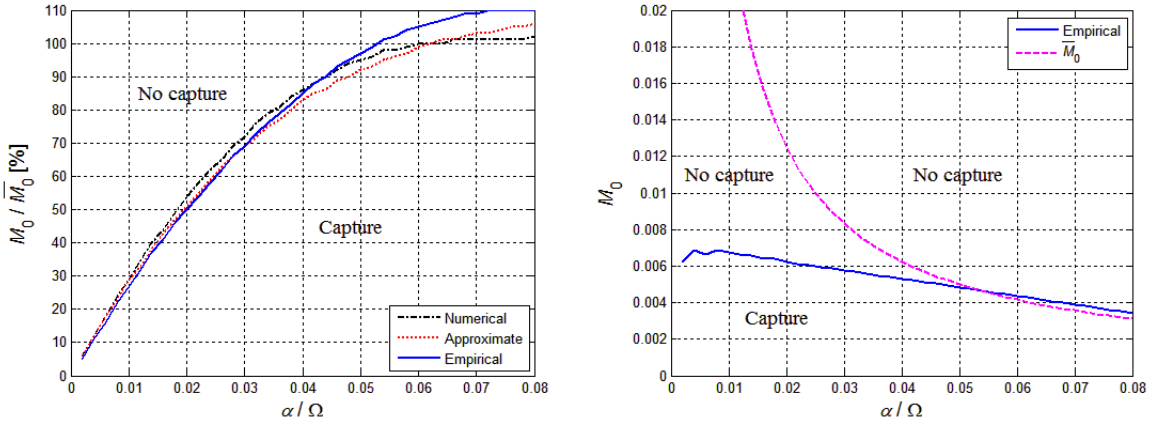

Figure 6 Capture / no-capture discriminant function (left) and comparison with the "limit" value $\overline{M}_0$ (right).

Through almost-stationary techniques, it can be stated that the capture condition shows the following characteristics:

- it can take place only close to the system translational resonance and strongly depends on the viscous damping, which balances the energy introduced in the system by the external torque;
- when damping is small, the capture condition occurs for external torques much smaller than the "limit" value determined with an almost-stationary approach, while for large values of the damping the two conditions are nearly coincident. This behaviour can be explained considering the duration of the system transient and consequently depends on the initial conditions.

The substantial objective has been reached with the definition of a criterion that allows foreseeing the capture condition depending on external torque and system damping, without having to perform the numerical integration of the nonlinear differential equations. Hence this approach may represent a useful tool in the engineering design of rotors.

REFERENCES

[1] Nayfeh H., Mook D. T., *Nonlinear oscillations*. John Wiley, New York, 1979.

[2] Quinn D.D., Resonance capture in a three degree–of–freedom mechanical system. *Nonlinear Dynamics*, 14, pp.309–333, 1997.

[3] Dimentberg M.F., McGovern L., Norton R.L., Chapdelaine J., Harrison R., Dynamics of an unbalanced shaft interacting with a limited power supply. *Nonlinear Dynamics*, 13, pp.171–187, 1997.

ISSN 1590-8844
International Journal of Mechanics and Control, Vol. 11, No. 02, 2010

MECHANIZATION OF THE HARVESTING OF MYRTLE BERRIES (*Myrtus communis L.*)

F. Paschino F. Gambella

Department of Agricultural Engineering, University of Sassari, Viale Italia 39, 07100 Sassari, Italy

ABSTRACT

The growing demand for myrtle berries for use in the production of liqueurs is at present being met through direct harvesting from spontaneous plants. The difficulty of harvesting berries from plants that differ greatly in shape and size requires a large expenditure of labour which leads to high production costs. However, besides the need to increase the availability of berries, in order to reduce costs it is necessary to use proper harvesting systems that are respectful of plants and fruit, but which are most of all capable of facilitating harvesting. The present study compares the results of different harvesting tests on low-, medium- and high-growing plants with a combing machine powered by a generator and a portable battery.

Keywords: harvest, combing machine, collecting systems, myrtle berries.

1 INTRODUCTION

Several species of small fruits are important commercially. Myrtle (*Myrtus Communis L.*) is a typical representattive of the Mediterranean flora which spontaneously develops in Italy, Spain, France, Tunisia, Algeria and Morocco. In Italy is present in almost all the coastal zones and principally in islands [1]; [2]. In the folk medicine leaf and fruit, are used for oral, internal and external diseases [3] [4]. The myrtle fruit is a berry, to spherical or ellipsoidal form and its colour can range from the dark red to the purple and to the white. The fruits are used especially in Sardinia in the preparation of a well-known liqueur (red myrtle) obtained by cold water and alcohol infusion of the berries. In the last few decades the production of this liqueur has increased by about 6%, from 170,000 to 180,000 litres per year. The harvesting of berries from spontaneous plants is performed exclusively by hand using small combs with bags underneath to catch the berries [5]. In harvesting by hand, from two to three persons per plant are required for a total from two to three and a half hours of work with a yield of 100% from the single plants [6]; [7]. An adult hand picking into a bag may harvest only from 2,5 kg/h to 4 kg/h of berries [8].

Contact author: Francesco Paschino, Filippo Gambella[1]

Department of Agricultural Engineering, University of Sassari, Viale Italia 39, 07100 Sassari, Italy
phone: +39 079 229281 – fax: +39 079 229285
Email: [1] gambella@uniss.it

Thus we have a high labour cost that represents over 70% of the entire cost of the production cycle with low working capacity and excessive damaging of the raw material. To increase harvesting efficiency, the most prolific branches are cut off and taken to where hand picking of the berries is facilitated. If this work were performed by skilled personnel, the consequences would not be serious, but unfortunately this is most often not the case and thus there is the risk of damaging plants and reducing future production. Only recently has the economic importance of myrtle been understood and this has stimulated entrepreneurs to adopt the rational production of myrtle berries through cultivation of the plant; this has seen a noteworthy increase, going from 101 to 476 hectares in the last few years. This positions Sardinia as the leading region in the cultivation of myrtle. This has led to considering the opportunity of cultivating the plant using traditional farming operations (pruning, lopping, fertilization and irrigation) and calling for the mechanical harvesting of the berries to increase yields and consequently also the working capacity of those employed in harvesting. From this standpoint, the mechanization of myrtle berry harvesting by electrical rotating comb has become a primary objective in reducing production costs, increasing the harvest of product collected for hour and for worker and at the end for increasing profits. The aim of the work is to evaluate the harvest times and the work capacities in worksites harvested with battery-powered combing machine with nets on the ground below the canopy (Sella & Mosca and Pozzo D'ussi) and worksite harvested with generator-powered combing machine with espalier nets

(Castelsardo) on plants with different height (high, medium and low) and so as to optimize performance and guarantee a high quantitative and qualitative level of the final product.

Table I - Varieties and production per plant of the myrtle bushes cultivated at Sella & Mosca, Pozzo d'Ussi and Castelsardo.

Site	Variety	Cultivation		
		production (kg/plant)	plant (density/ ha)	height plant (m)
Sella & Mosca	RUM 14	0.95	4000	2.4
Pozzo d'Ussi	RUM 4	0.83	4166	1.6
	CPT 5	0.69	4166	1.5
Castel-sardo	ISILI	0.84[(a)] – 1.29[(b)]	5000	0.9
	CPT 3	0.51	5000	1.2
	SBD	0.40	5000	1.1

(a) referring to production per plant obtained from harvesting with the type b technique
(b) referring to production per plant obtained from harvesting with the type c technique

2 MATERIALS AND METHODS

2.1 TEST SITES

Tests were performed at three sites, two in the Nurra region of Sassari and Porto Torres and one at Castelsardo. The first site, on lands belonging to the Sella & Mosca Company, is a myrtle field including a total of twelve varieties on an overall area of approximately one hectare, with height plants (2,5 m) and eight years old, spaced 2.5 by 1 metre, trained in bowl form and drip irrigated. The second site, called "Pozzo d' Ussi " contains 17 varieties, with plants of medium height (1.6-1,5 m), of four years old and trained to bowl shape, spaced 2 by 1.2 metres. Finally, the third site was in the municipality of Castelsardo, contains 7 varieties with plants of low height and of two and four years trained to bowl shape and spaced 2 by 1 metres. The varieties submitted to the harvesting test (Table I) were six overall, of which one at Sella & Mosca (RUM 14), two at " Pozzo d'Ussi " (RUM 4 and CPT 5) and three at Castelsardo (Isili, CPT 3 and SBD). Production per plant varied from site to site: with RUM 14 at Sella & Mosca, production was 0.95 kg/plant; with RUM 4 and CPT 5 at "Pozzo d'Ussi" 0.83 kg/plant and 0.69 kg/plant, with plants harvested with two the techniques a) and d): battery-powered combing machine with nets on the ground below the canopy (Figure 1 and 4). At Castelsardo all the plant have a low high, with ISILI there was a production of 0.84 kg/plant and 1.29 kg/plant, referring to plants harvested with one different techniques: b) and c): generator-powered combing machine with espalier nets (Figure 2 and 3); with CPT 3 and SBD, there was a yield of 0.51 kg/plant and 0.40 kg/plant.

Figure 1 Type a) worksite with battery-powered combing machine and nets on ground under the canopy.

Figure 2 Type b) worksite with battery-powered combing machine and espalier nets.

Figure 3 Type c) worksite with generator-powered combing machine and espalier nets.

Figure 4 Type d) worksite with generator-powered combing machine and nets on ground below the canopy.

3 MACHINERY EMPLOYED

The machine employed is a combing machine produced by the COIMA Company, model 105 C "Olivella Mini", weighing 1.2 kg; it has a rigid telescopic shaft with a length of 70 cm that can be extended from 1.60 to 2.90 cm for work on plants of large dimension, and an ergonomic grip that can be turned through 180°. At one end is the working head composed of a 12-volt electric motor with an on/off switch and a comb with a working width of 17.5 cm on which are mounted eleven undulating, counter-rotating titanium teeth, each some ten cm in length and covered with a silicon sheath up to 9 mm in diameter to allow a useful distance of 6.5 mm. Powering of the combing machine is supplied by a 1 kW generator placed in the open field or by a backpack battery having an overall weight of 5 kg. For the worksites 1 and 2 the electrical comb was connected with a prolongs to 25 meter maximum length to the generator. The worker could freely proceeding to the collection for a length to spin equal to the length of the extension and the end had to go back to the field head move the generator and begin the harvest again. All that created a slowing down harvest work and increase some partial times of work, to move among the plants and free the extension which was getting entangled in the shrubs, and later the total work time. In the other two worksites instead, operators were gifted with a battery taken to life by a special sling. All that was allowing the workers to move more nimbly between the myrtle plants without having to go back to the field head to move the electrical generator or move among the plants to disentangle the extension thread. The work capacity of the individual workers was calculated as: **Work capacity per worker** (kg/h) = Operational Capacity (OC)/number of worker; where **OC** (operational capacity of the single worker) was calculated as a function of **OT** (Operational Time) and **AT** (Additional Time). **OT** is the working time of the worker and was calculated as the sum of the effective time (**ET**) and the additional time (**AT**).

3.1 WORK AREAS

The work cycle was performed normally in four stages: placing of the product collector a net placed underneath the canopy or an espalier net, detachment of the berries, rolling up of the net under the canopy and discharging of the berries into 25-kg plastic crates. Tests were performed by harvesting the berries from plants having different heights: low <1 m (ISILI), medium <1.6 m (CPT 3, CPT 5, RUM 4 and SBD), high >1.6 m (RUM 14) and comparing the results obtained at four different worksites:

a) battery-powered combing machine with nets on the ground below the canopy (Figure 1);
b) battery-powered combing machine with espalier nets (Figure 2);
c) generator-powered combing machine with espalier nets (Figure 3);
d) generator-powered combing machine with nets on the ground below the canopy (Figure 4).

The nets below the canopy were laid on both sides of the row over a distance of 10 metres, while with the espalier nets the length was 1.5 metres. One worker harvested the berries from the single branches by "combing" with the machine and allowing the berries to fall into the net. Then, together with another worker, the berries were placed in the crates.

4 RESULTS AND DISCUSSION

4.1 WORKING TIMES

Analysis of working times obtained (Table II) shows the noteworthy variability found at the different experimental worksites which resulted in a marked difference in working times on the single plants. These were particularly influenced by accessory times and especially by the time spent handling the nets. In fact, at the sites with nets on the ground underneath the canopy,

the time consumed in handling them strongly influenced operating times; with reference to the single plants, times varied from a minimum of 2.4 minutes to a maximum of 11.3 minutes in the different worksites and for plants of different heights. Analyzing in detail the times per plant, the lowest values, from 2.4 to 4.3 minutes, were obtained at the sites where the espalier nets were used while with nets on the ground times were from 7.9 to 11.3 minutes per plant.

Table II - Total and per plant working times obtained at the different worksites

Variety	Work site	Production	Work site		Work capacity		Labour productivity per wo		
			Referring to ET		Referring to OT		Referring to ET		Referrin
		(kg/ha)	plants (n/h)	product (kg/h)	plants (n/h)	product (kg/h)	plants (n/h)	product (kg/h)	plants (n/h)
RUM 4	a	3457.8	32.6	27.0	7.5	8.0	16.3	13.5	3.8
CPT 5	a	2875.5	29.6	20.4	7.6	12.5	14.8	10.2	3.8
ISILI	b	6450.0	20.6	26.6	14.1	18.2	10.3	13.3	7.1
SDB	b	2000.0	42.3	16.9	24.6	9.8	21.2	8.5	12.3
ISILI	c)	4200.0	23.0	19.3	16.9	14.2	11.5	9.7	8.5
CPT 3	c)	2200.0	54.1	23.8	25.1	11.0	27.1	11.9	12.6
RUM 14	d	3800.0	11.5	11.0	5.3	5.0	5.8	5.5	2.7

This was true even with plants below the height of 1.6 metres and did not vary with the type of power supply used (generator or battery). In particular, at the worksite with the battery-powered combing machine operating on medium-sized plants with nets on the ground underneath the canopy, the times were 8.0 and 7.9 minutes respectively for plants of the RUM 4 and CPT 5 varieties with the same kind of worksite, but on plants 2.4 metres high (RUM 14) the time was the longest, with 11.3 minutes per plant. However, in the two work sites with espalier nets on plants of the low-growing ISILI variety, the time per plant was 3.5 and 4.3 minutes; in the SBD and CPT 3 varieties of medium height the time was about 2.4 minutes. In reality, it was the handling of the nets that conditioned the work of personnel, with an incidence of 78% with nets on the ground underneath the canopy while with espalier nets the percentage was below 62%. Consequently, operating efficiency was greater at worksites where operating times were shorter: b) and c) ISILI with 68.2% and 73.7%, despite the presence of the power generator which with its power cable hindered workers; the lowest was 22.9% in work site a) with the RUM 4 variety. In conclusion, operating times were extremely variable, from minimum values of 155.5 h/ha at worksite c), CPT 3, to maximum values of 755.4 h/ha at worksite d), RUM 14.

4.2 WORK CAPACITY

Work capacity was directly related to working times and production per plant and marginally to plant spacing, that is, plantation density. The values obtained refer to effective time (TE) and operating time (TO) in order to evaluate the influence of accessory times (TA) on worksite capacity and consequently on labour productivity. On observing the results (Table III), we can clearly see the difference in capacity of the worksites in which we find the highest and lowest plants; those with nets underneath the canopy and the espalier nets and those with the highest and lowest production.

In reality, at work site c), with the CPT 3 variety, work capacity reached 54.1 plants per hectare with reference to TE and only 25.1 plants per hectare with reference to TO. At worksite d), with the RUM 14 variety, the aforementioned values were reduced to 11.5 and 5.5 plants per hectare. In this case, the large difference (-46%) is to be attributed substantially to plant height, which in RUM 14 was over two metres (2.4 m), while with CPT 3 the average height was 1.2 metres. If we then consider mean production per plant, this is decidedly favourable to the ISILI variety, 0.84 kg/plant and 1.29 kg/plant compared to 0.40 kg/plant with SBD, which presents a marked difference in the capacity values: 14.2 kg/h with ISILI and 9.8 kg/h with SBD, despite being in the same harvesting site. As concerns the system of berry collecting, the use of espalier nets afforded the best results owing to the ease with which they could be moved and repositioned under the plants compared to nets on the ground underneath the canopy. The differences are highly significant in TA, with increases in capacity above 60% on the average.

Table III - Work capacity and labour productivity relating to tests performed at worksites a), b), c), d)

Variety	Work site	Working times: ET	AT: Net Handling	AT: Shifting from plant to plant	Total	OT	Operative Efficiency ET/OT	Time per plant
		(h/ha)	(h/ha)	(%)	(h/ha)	(h/ha)	(h/ha)	(%)	(min)
RUM 4	a	127.9	338.4	78.7	91.8	430.4	558.2	22.9	8.0
CPT 5	a	140.8	322.4	78.5	88.1	410.5	551.4	25.5	7.9
ISILI	b	242.3	67.6	59.9	36.2	113.0	357.3	68.2	4.3
SDB	b	118.1	52.9	62.0	32.4	85.3	203.5	58.1	2.4
ISILI	c)	217.7	46.6	60.0	31.2	77.7	295.4	73.7	3.5
CPT 3	c)	92.4	66.3	62.0	40.6	107.0	199.5	46.4	2.4
RUM 14	d	346.4	318.0	77.8	113.6	408.9	755.4	45.9	11.3

a) battery-powered combing machine with nets on the ground below the canopy; b) battery-powered combing machine with espalier nets; c) 1kW generator-powered combing machine with espalier nets; d) 1kW generator-powered combing machine with nets on the ground under the canopy. * two workers per worksite

Although the values of labour productivity show the same trend as those for worksite capacity, show values that are certainly more interesting, especially with espalier nets. In fact, at worksites a) and d), productivity referring to TE was 16 plants per hectare against the 3.8 plants per hectare referring to TO; comparing them to production we have 13.5 kg/man-hour and 4.0 kg/man-hour, even in this case

the reduction was substantial considering the product harvested (-77%) and the number of plants (-70%). At worksites b) and c) the values obtained were noteworthy, going from 4.9 kg/man-hour to 9.1 kg/man-hour which, referring to the number of plants, went from 13.3 to 7.1 plants/h.

The average harvested yield reached 100% with medium- and small-sized plants while it was slightly above 95% at worksite d) where, for large plants, a telescopic shaft was added to the combing machine and this made harvesting more difficult.

Generally speaking, the weight of berries and the force needed to detach them played a significant role since the combing action, although to a limited extent, is essentially based on the resistance of the pedicel. In fact, the force required to detach the berry is dependent on its size and weight. The analyses performed in the course of specific tests have shown that on harvesting dates subsequent to the tests illustrated herein there was a reduction in detachment force as a function of weight class, with reductions more marked in the weight classes below 0.30g (-64%) and to a lesser extent in those of greater weight (-53%).

5 CONCLUSIONS

Considering the results obtained, it appears evident that the use of the combing machine for the harvesting of myrtle berries from plants is certainly possible. Obviously, the best results are connected with specific plant agronomic and structural factors, high plant production, height of plants not above 150 cm, a good size of berries and low detachment force values are certainly at the basis of obtaining satisfactory work capacity. It is not by chance that the highest work capacity was reached at the site with the highest production (6450 kg/ha). To these aspects must be added consideration for planning with the utmost attention the composition of the work sites which, as has been underscored several times also in the course of this work, significantly condition the performance of harvesters. The generator- or battery-powered combing machine had little effect on workers' productivity, while the kind of collector, espalier nets and not ground nets, led to high work capacity and similarly excellent labour productivity owing to the easier handling of the nets. In reality, it was the incidence of accessory times that strongly conditioned the final result and the difference in the values obtained induce us to experiment in further detail to define a more efficient system of collection. Finally, the introduction of the combing machine certainly assumes an important meaning in economic terms since it enhances the market possibilities of the product, but most of all represents an important aspect in the safeguarding of the environment in general and of myrtle in particular by subtracting it from insistent anthropic pressure for its economic exploitation.

REFERENCES

[1] Tutin et al, *Flora Europea*. Cambridge University Press, Cambridge, 1964.

[2] Pignatti, *Flora d'Italia*. Edagricole, Bologna, 1982.

[3] Khosh-Khui et al, Micropropagation of myrtle (Myrtus communis L.), *Scient. Horticultur*, 22, pp. 139-146, 1984.

[4] Milhau et al, In vitro antimalarial activity of eight essential oils, *J. Essential Oil Res*, 9, pp. 329-333, 1997.

[5] Paschino F., Gambella F., Meccanizzazione della raccolta delle bacche di mirto (*Myrtus communis L.*), Report presented to the Congress "Mirto di Sardegna tra tradizione e innovazione", Cagliari, 7 December 2006.

[6] Paschino F., Gambella F., Pinna G., La meccanizzazione della raccolta del mirto, *Proceedings Third Day of Study on Myrtle*, Sassari, pp. 43-50, 23 September 2005.

[7] Gambella F., Paschino F., Meccanizzazione della raccolta delle bacche di mirto (*Myrtus communis L.*), *Proceedings Convegno AIIA 2005: "L'ingegneria agraria per lo sviluppo sostenibile dell'area mediterranea"*, Catania, 27-30 June 2005.

[8] Peterson D.L., Wolford S.D., Mechanical harvester for fresh market quality steamless sweet cherries, *Transactions of the ASAE*, Vol. 44(3), pp. 481-485, 2001.

The authors have contributed equally to the preparation of the present paper.

Work performed within the framework of the research project entitled "Macchina per la raccolta delle bacche di Mirto" financed by the Autonomous Region of Sardinia (RAS), Council for Agriculture and Agro-Pastoral Reform.

ISSN 1590-8844
International Journal of Mechanics and Control, Vol. 11, No. 02, 2010

A STUDY ON BALANCE ERRORS IN PNEUMATIC TYRES

Marco Ceccarelli* Alessandro Di Rienzo* Giuseppe Carbone* Piero Torassa**

* LARM Laboratory of Robotics and Mechatronics, DiMSAT - University of Cassino
Via Di Biasio, 43 - 03043 Cassino (Fr), Italy - E-mail: {carbone, ceccarelli}@unicas.it

** Research and Development Department, Marangoni Tyre S.p.A.
Via Anticolana, 32 - Anagni (Fr), Italy - E-mail: p.torrassa@marangoni.com

ABSTRACT

This paper has reported results of an investigation on main possible sources of unbalance in design and manufacturing process of pneumatic tyres. Main characteristics of a tyre, its components, and assembly operations are analyzed by referring to a production line at Marangoni Tyre plant in Anagni, Italy. Numerical models are proposed and implemented for identifying and quantifying the contribution of main sources of unbalance within an overall unbalance of built tyres. A procedure is also proposed for an experimental validation of the proposed numerical models. Experimental tests have been reported to validate both the proposed procedure and results of the numerical models.

Keywords: Tyres, Balance Errors Analysis, Numerical models, Experimental tests.

1 INTRODUCTION

The wheels of all modern vehicles are equipped with pneumatic tyres. Tyres support the vehicle and transmit power by contact among wells and ground, [4]. Main characteristics for tyres are comfort running, keeping road, robustness, duration, and transmission of the generated forces to the ground, [8].
Today production technology and manufacturing process of tyres are characterized by a high level of standardization. The tubeless technology, that was introduced by Goodridge in 1947, permits to travel more in case of drilling failures. In addiction, the radial ply, that was introduced by Michelin in 1948, gives to a tyre a differentiated rigidity to the tread and to the sidewall that permits to have an optimized imprint on the ground, [3]. All modern tyres are tubeless and include radial ply manufacturing technology. The types of rubber that are used and the design of the tread are the main characteristics that differ tyres of different producers.
Tyre balance is strictly related to the equilibrium of a wheel. Unbalanced wheels give ride disturbance to the vehicle and can generate irregular wear of mechanical components. Counterbalance masses are used for balancing of the wheels. Thus, a high quality standard in the production of the tyres requires minimum balancing errors.

Contact author: Marco Ceccarelli

E-mail: ceccarelli@unicas.it.

It permits to have maximum performance in term of dynamic behavior, especially at high speeds. Since 07/01/2006, the European Directive 2000/53/CE prescribes illegal the marketing and the application of counterbalance masses made of lead in vehicles in order to limit the use of harmful materials, [6]. Alternative materials are zinc, steel or tin, which show smaller density and a minor specific mass. Thus, a balance mass will have larger volume when made of these materials.
Thus, it is fundamental importance to identify and to model unbalance sources in order to understand and to conceive solutions for correcting or preventing large balance errors.

2 PNEUMATIC TYRES AND THEIR PRODUCTION PROCESS

Tyres are composed of several elements as shown in the scheme of Fig. 1. The main components are [5]: the tread, the body ply, the belts, the bead, and the liner tread.
The tread consists of special rubber, which has the purpose to transmit forces between tyre body and ground. It also ensures wear resistance, cut resistance, heat resistance, low rolling resistance, or any combination of these [5].
The body ply of a radial tyre is made of a single layer of textile wire that runs from bead to bead orthogonally to the direction of motion (hence the term "radial plies"). The body ply transmits the forces from the belts to the bead and eventually to the rim, and it restricts the air pressure, which ultimately carries the load.
Belts are layers of steel cord wires that are located between

the tread and the body ply. The steel wire of the belts runs diagonally to the direction of motion. Belts increase the rigidity of the tread, which increases the cut resistance of tyre. They also transmit the torque to the radial ply and restrict tyre growth, which prevents cutting, cut growth and cracking [5].
The bead of a cross-ply tyre consists of bundles of bronze coated steel wire strands, which are covered with rubber. The bead is considered the foundation of the tyre. It anchors the bead on the rim.
The liner tread consists of special mixture, which gives the property of impermeability to air and water in a tyre.
Tyres are built in standard dimensions to allow the correct coupling with rims. These are marked on the side of the tyre together with commercial and technical informations, as shown in the scheme of Fig. 2, [2].

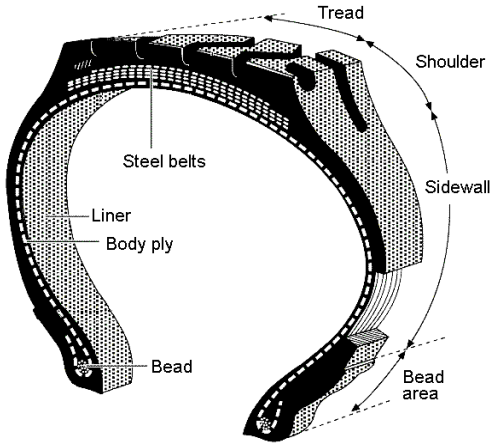

Figure 1 Scheme of main components of a tyre with radial structure [3].

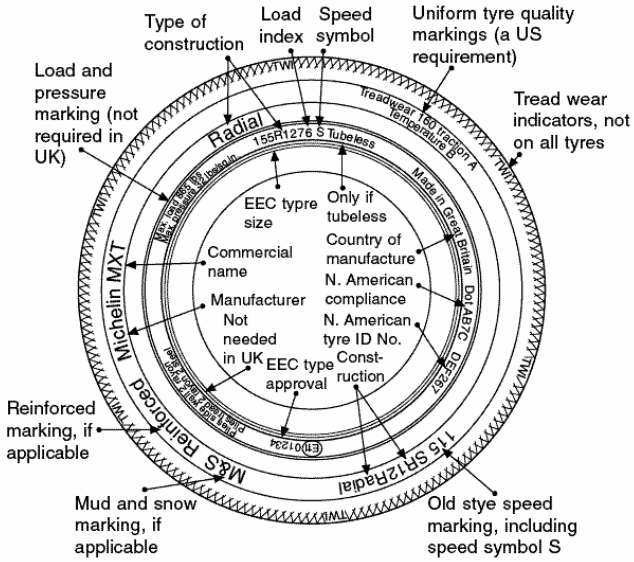

Figure 2 Main characteristics as stamped on the side of a tyre [3].

Commercial informations are the model of a tyre, the brand and the logo. In addition, main technical informations are dimensional and constructive characteristics, the maximum load and velocity, [8]. Dimensional characteristics are the width of the section of the tyre (in millimeters), the shape ratio given by the height of the section divided by the width and multiplied for a hundred, and finally the diameter of the rim (in inches). A constructive characteristic is the angle of the cords with respect to the direction of motion. Modern tyres are made of radial structures, with tube or tubeless solution, [8].
The process of production of a tyre can be summarized in the following steps [7]: the mixing, the calendering, the tread and sidewall extrusion, the bead construction, the tyre assembling, the curing, the trimming, and the inspection.
During the mixing production process several grades of natural and synthetic rubbers are combined in a closed mixer (the banbury, shown in Fig. 3 (a)). Then they are mixed with black carbon and a cocktail of other chemical products that enhance the characteristics of the rubbers. In order to obtain good uniformity in terms of composition and density, rubber is twisted and lengthened in an open mixer that is composed by big rollers as shown in Fig. 3 (b).

(a)

(b)

Figure 3 Mixers at Marangoni Tyre plant in Anagni: (a) closed mixer; (b) open mixer (courtesy of Marangoni Tyre S.p.A).

(a)

(b)

Figure 4 Manufacturing machines at Marangoni Tyre Plant in Anagni: (a) tread extruder; (b) building tyre machine with two-stage process (courtesy of Marangoni Tyre S.p.A).

In calendering process a textile wire or steel cord is woven to create a complex textile support that is later coated with a film of rubber on both sides. Calendered textiles such as rayon, nylon and polyester are used for the body ply. Steel cords are used for belts, [7].

The tread and sidewalls are produced by forming two (or more) different and specifically designed compounds by feeding the rubber through an extruder. Extruders produce continuous beams of tread rubber, or sidewall rubber as shown in Fig. 4 (a).

In the bead construction process the bead core is constructed by coating bronze high tensile strength steel wire, which is wound on a bead former by a given number of turns to provide a specific diameter and strength for a particular tyre.

Tyre assembling is traditionally a two step process as shown in Fig. 4 (b). In the first step, the liner, body plies and sidewalls are placed on a building drum. Then beads are positioned, ply edges are turned around the bead core and sidewalls are simultaneously installed into position. In the second tyre building step, the tyre is shaped by a mechanic drum. Then two belts and the tread layer are added. At the end of this step, the tyre is named as a "green tyre". The "green tyre" has no tread pattern and no markers. It is simply a bare rubber casing.

During the vulcanization process the green tyre is placed in a mould inside a vulcanization press and is vulcanized for a specific duration of time at a specific pressure and temperature, as shown in Fig. 5 (a). Each curing press is equipped with an interchangeable set of moulds, but it will press only one tyre of one size and pattern at a time. The finished tyre is then ejected from the mould.

In trimming and inspection processes, operators remove the excessive rubber from the cured tyre and inspect the quality of the tyre. During the inspection process the tyre is inspected for uniformity with appropriate machines as shown in Fig. 5 (b) and finally it goes to the dispatch warehouse.

(a)

(b)

Figure 5 Manufacturing machines at Marangoni Tyre Plant in Anagni: (a) Curing press ; (b) a measure station (courtesy of Marangoni Tyre S.p.A).

3 THE BALANCE PROBLEM IN PNEUMATIC TYRE

A correct balancing of wheels permits to preserve shock absorbers, bearings and steering component of wheels as well as to obtain a regular wear of tyre and at the driving comfort as pointed out in [8].
The unbalance of wheels is given by radial force (F_Z), lateral force (F_Z), tangential force (F_Y), camber moment (M_X), steering moment (M_Z) and rolling resistance moment (M_Y), as shown in Fig. 6. These disturbances are directly proportional to the velocity of the wheel [1]. Tyre unbalance is given by no symmetrical distributions of weight [8]. The unbalance state of a tyre is known as dynamic unbalance, and it is given as the sum of static and couple unbalance of a tyre [1].

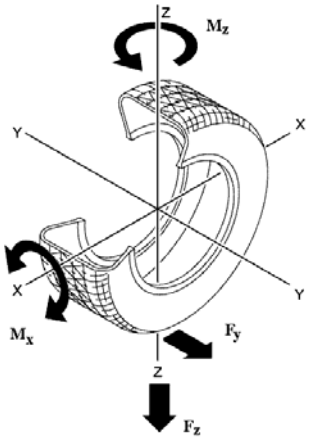

Figure 6 Actions generated during the rolling of an unbalance wheel.

The static balance condition is verified when the sum of static moments is zero [8]. This case can be expressed for each mass i as

$$\sum_i M_{si}=F_{si}b=m_i g b=0 \quad (1)$$

where M_s is the static moment given by the product of a static force F_s by the distance b to the centre of the tyre (b), as shown in Fig 7(a). F_s is given by the product of an unbalance weight m for the gravity acceleration g, and i is the number of unbalanced weights in the tyre.
Static unbalance can be modeled with a lumped mass in the equatorial plane. This causes a vertical oscillation of the wheel, and therefore a bouncing sensation can be experienced by a passenger, as shown in Fig. 7, [8].
In a tyre with a couple unbalance, the sum of inertial centrifugal forces is zero, but the sum of inertial moment that is generated by them is not zero, as shown in Fig. 8 (a). Inertial centrifugal forces are balanced when

$$\sum_i F_{ci}=m_i\omega^2 r_i=0 \quad (2)$$

where F_c is the centrifugal force that is generated by the rotation of a mass m about the rotation axis, with distance r to it and at velocity ω, and i is the number of unbalanced weights present in the tyre.

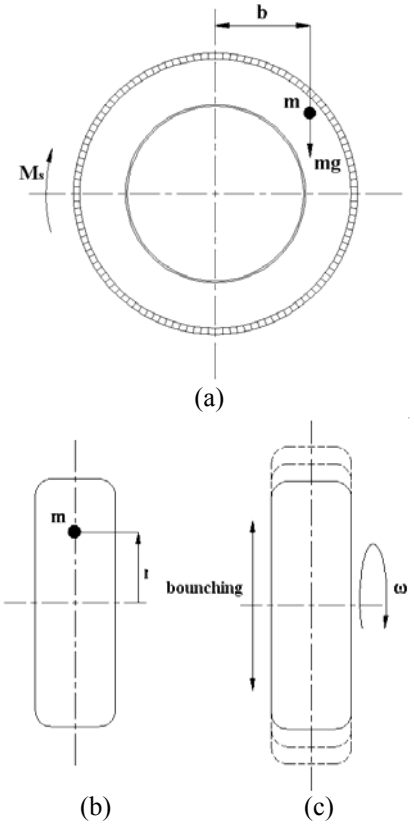

Figure 7 A scheme of a static unbalanced tyre: (a) meridian view; (b) radial view; (c) bouncing oscillation during a motion [8].

Inertial centrifugal moment is given by the sum of couples that are generated by the centrifugal forces when

$$\sum_i M_{ci}=F_{ci}a\neq 0 \quad (3)$$

where M_c is the centrifugal inertial moment given by the product of a centrifugal force (F_c) with the distance from the equatorial plane of a tyre.

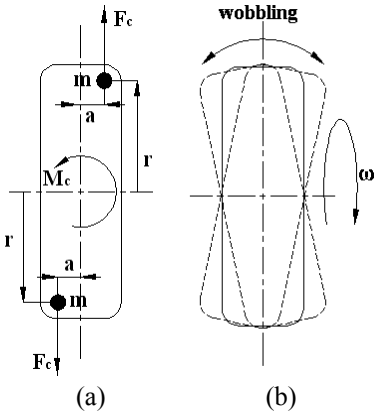

Figure 8 A scheme of: (a) couple unbalanced tyre; (b) oscillation during a motion [8].

Couple unbalance can be simulated by two lumped masses that are placed in opposite planes in opposing directions. This gives a transversal oscillation during the motion that causes a wobbling sensation for the passenger, as shown in Fig. 8 (b), [8].
The combination of static and couple unbalances gives a dynamic unbalance. In this case, the sums of static moments, inertial forces and inertial moments are not zero. Dynamic unbalance can be modeled with a lumped mass that is located away from rotation axis and equatorial plane, as shown in Fig. 9 (a). This mass causes vertical and transversal oscillations of the wheel. The passenger has sensations of bouncing and wobbling as shown in Fig. 9 (b), [8].
A wheel is balanced if it is in dynamic equilibrium. In fact, dynamic balancing is also a guarantee for static balancing. Balancing permits to reduce vibrations of the wheel and therefore it limits ride disturbance and damages of mechanical components. It can be obtained by means of at least two masses, as counterbalance masses, at suitable locations, [8].
A pneumatic tyre can be modeled by means of two coaxial and parallel disks. Static and couple unbalance can be modeled by means of two masses that are located on the disks, as shown in Fig. 10. In static unbalance the masses are placed symmetrically with respect to an equatorial plane. In addiction, they are located anti-symmetrically in the case of couple unbalance [1].
Dynamic unbalance is obtained when suitable masses are installed in the disks for static and couple unbalancing. This can be modeled with four masses that are placed in the disks. Two are located symmetrically and other two anti-symmetrically. Balancing is obtained by placing at least a counterbalance in each disk as shown in Fig. 11, [1].

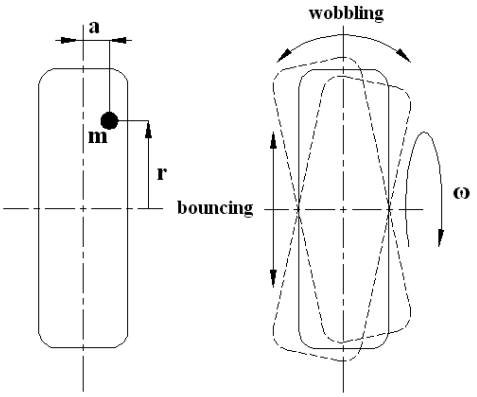

Figure 9 A scheme of: (a) dynamic unbalanced tyre; (b) oscillation during the motion [8].

Tyre can be analyzed like a rotor. A rotor has three principal axes of inertia, and it can turn around them in condition of dynamic equilibrium, when

$$\sum_i F_{ci}=0 \text{ e } \sum_i M_{ci}=0 \quad (4)$$

Thus, unbalance can be checked when rotation axis does not coincide with one of inertial axis [8].
In static unbalance condition the centre of mass and the axis of inertia are translated with respect to the axis of rotation of a tyre, as shown in Fig. 12 (a). In couple unbalance condition the centre of mass is on the axis of rotation but the axis of inertia is tilted with respect to it, as shown in Fig. 12 (b). In dynamic unbalance condition the centre of mass is shifted along the axis of rotation and away from equatorial plane; the axis of inertia is shifted and tilted with respect the rotation axis, as shown in Fig. 12 (c). Balancing makes coincident the axes of inertia and rotation, and place the center of mass in the center of a tyre, as shown in Fig. 12 (d), [8].

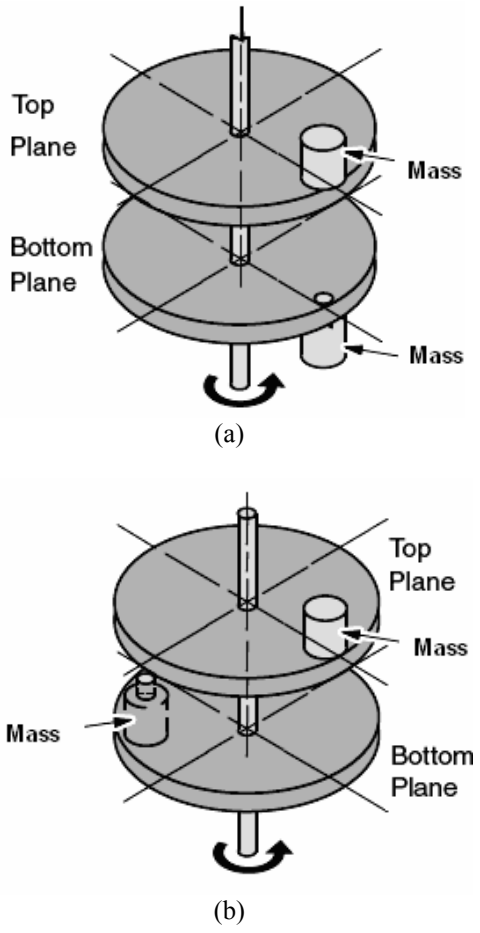

Figure 10 Model for unbalance of a tyre: (a) static case; (b) couple case [1].

4 SOURCES OF UNBALANCE

An analysis of composition and manufacturing of tyre production can be useful to identify unbalance sources.
In particular, the following unbalance sources can be identified:

- Radial dissymmetry of weight of one or more layers;
- Axial dissymmetry of weight of one or more layers;
- Disuniformity of density of one of more layers;
- Inhomogeneity of elastic strain in dynamic behavior.

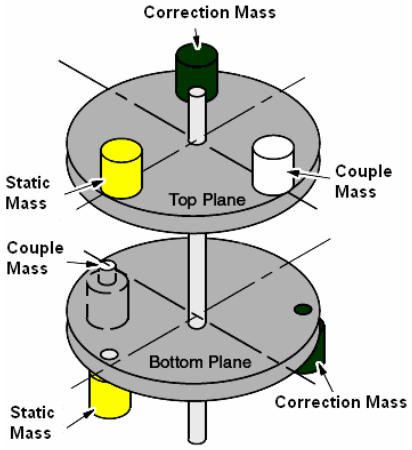

Figure 11 A model with masses for balancing a tyre [1].

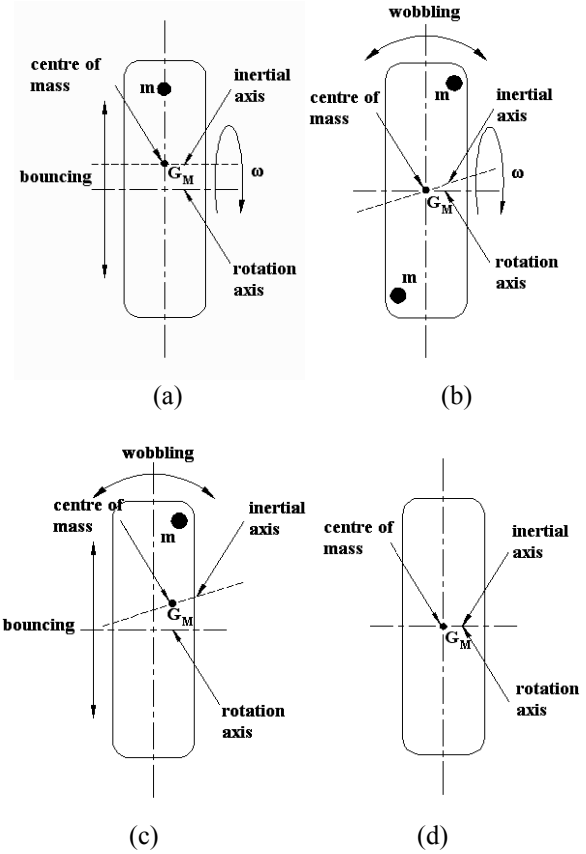

Figure 12 Position of the center of mass and inertial axis with respect to a rotation axis in condition of: (a) static unbalance; (b) couple unbalance; (c) dynamic unbalance; (d) balanced tyre [8].

Radial dissymmetry can be given by a discontinuity due to a junction of a layer, which is usually obtained with an overlap of edges. A local thickening given by production process and an erroneous placement of layers can also cause a radial dissymmetry. However major causes can be considered an overlap of edges and an erroneous deposition.

Axial dissymmetry is mainly given by a layer that is not centered in the equatorial plane of a tyre. The overlap of edges, discontinuity defect, and an erroneous deposition can cause an axial dissymmetry.

Density disuniformity can give dissymmetry in mass distribution and can be caused by an irregular distribution of material or by chemical structure variation in one or more layers.

Uncontrolled tensioning of a layer deposition can causes localized laps, crests, or strictions in a deposited layer.

Inhomogeneity of elastic strain can produce a different axial and radial behavior of one or more layers of material during dynamic operation. Inhomogeneity can be produced or amplified also by dissymmetrical distribution of masses.

A different cooling of tyre components can give distortions and consequently residual states of stress.

A single layer can influence the final state of unbalance of a tyre, especially if it has weight, thickness, and axis distance larger than in other layers.

An analysis of a product and its manufacturing process permits to identify major causes for an unbalance of a tyre as in the following situations:

- Not centered position of a layer;
- Overlap of edges in a junction;
- Design of the tread;
- Erroneous location of beads;
- Geometry errors of molds;
- Distortion as given by differentiated cooling of the tyre;
- Distortion and/or dissymmetry of elements in a section of a tyre;
- Radial deposition error of a belt;
- Incorrect tensioning during deposition of belts;
- Ovality of beads;
- Inhomogeneity of material in terms of density, thickness, and molecular structure.

The above-mentioned unbalance sources can be significant and a suitable modeling and analysis can be useful to characterize tyre unbalance and to propose solution for it.

5 MODELS FOR NUMERICAL EVALUATIONS

Unbalance can be modeled with geometrical schemes by using lumped parameters as in Fig. 13. Schemes are reported to analyze situations which can accentuate or reduce final balance errors of tyres. In Figs. 14 to 21 main causes of unbalance are illustrated by emphasizing parameters that can be useful for theoretical and experimental characterization. In Fig. 13 is reported a scheme of an unbalance mass in a tyre.

Referring to Fig. 14, the overlap of edges in a junction gives an unbalance that can be expressed analytically as an unbalancing mass Δm_L, given by

$$\Delta m_L = \rho \, h \, L \, [t_L + 0{,}5 \, (s_L - t_L)] \qquad (5)$$

where ρ is the density of the material of layer; h represents the thickness; L, s_L and t_L are the dimensions that are shown in Fig. 14.
The radial and axial coordinates a and b, shown in Fig. 13, identify the position of the lumped mass. In case of overlap of edges they are indicated as a_L and b_L and are given from the geometry by following expressions

$$a_L = r + 0{,}5\ h \tag{6}$$

$$b_L = d_L + [0{,}5\ h\ (L\ t_L) + 0{,}33\ L\ (L\ 0{,}5(s_L - t_L))]\ h\ \rho\ /\Delta m_L, \tag{7}$$

where r is the radial distance from the centre of a tyre in a layer. In Fig. 14 is reported a scheme of an overlap of edges in a junction.
Referring to Fig. 15, the junction error gives an unbalance that can be expressed analytically as an unbalancing mass Δm_G. When $s_G < 0$ there is an overlap of edges in the junction and Δm_G is given by

$$\Delta m_G = \rho_c\ h_c\ L\ [t_G + 0{,}5\ (s_G - t_G)] \tag{8}$$

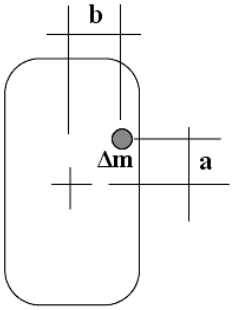

Figure 13 A scheme and coordinates of a lumped mass representing an unbalance mass in a tyre.

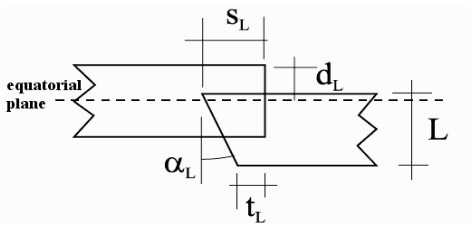

Figure 14 A scheme and parameters of overlap of edges in a junction (s_L: length of overlap; t_L: minimum length of overlap; d_L: shift of edges; α_L: angular deviation of head; L: width of a layer; h: thickness of a layer).

When $s_G > 0$ there is a distance of edges and Δm_G is given by

$$\Delta m_G = \rho_c\ h_c\ L\ s_G \text{ (with negative value)} \tag{9}$$

where ρ_c is the density of the layer using textile of steel cords; h_c represents the thickness; s_G e t_G are the maximum and the minimum overlap, like in the case of Fig. 14. In Fig. 15 is reported a scheme of confectioning junction of a belt with steel.

When $s_G < 0$ coordinates a_G and b_G that identify position of the error are given from the geometry by following expressions

$$a_G = r + 0{,}5\ h_c \tag{10}$$

$$b_G = d_G + [0{,}5\ L\ (L\ t_G) + 0{,}33\ L\ (L\ 0{,}5(s_G - t_G))]\ h_c\ \rho\ /\Delta m_G. \tag{11}$$

When $s_G > 0$ they are given by

$$a_G = r + 0{,}5\ h_c \tag{12}$$

$$b_G = d_G + 0{,}5\ L \tag{13}$$

where r is the radial distance from the centre of a tyre and d_G is shift of edges. Referring to the scheme shown in Fig.15, p_f and p_G represent the step of steel cords and the distance of steel cords in the junction.
Referring to Fig. 16, a local defect gives an unbalance that can be expressed analytically as an unbalancing mass Δm_d, given by

$$\Delta m_d = \rho\ h\ L_d\ s_d \tag{14}$$

where ρ is the density of the layer; h represents the thickness; s_d is the size of the defect and L_d is the axial dimension of the defect. In Fig. 16 is reported a scheme of a defect in a layer of a tyre.
The coordinates a_b and b_b that identify position of the error are given from the geometry by following expressions

$$a_d = r + 0{,}5\ h \tag{15}$$

$$b_d = d_d + 0{,}5\ L_d \tag{16}$$

where r is the radial distance to the centre of the tyre; d_d is the shift of the defect.
Referring to the Fig. 17, the tensioning error gives an unbalance that can be expressed analytically as an unbalancing mass Δm_t. When there is a striction for excessive tensioning it is given (with negative value) by

$$\Delta m_{ts} = \rho\ L\ h_t\ s_t \tag{17}$$

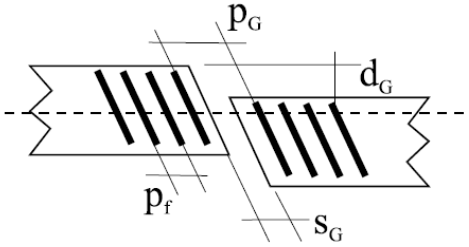

Figure 15 A scheme and parameters of confectioning junction of belt with steel assembly (s_G: distance or overlap width of a junction; d_G: shift of edges; p_f: step of steel cords; p_G: distance of steel cords in junction).

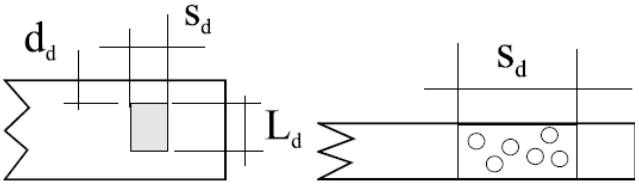

Figure 16 A scheme and parameters of a defect in a layer of a tyre (s_d: size; L_d: axial dimension; d_d: defect shift).

When there is an expansion for low tensioning it is given by

$$\Delta m_{tc} = \rho L h_t c_t \quad (18)$$

where ρ is the density of the defective belt; h represents the thickness of the belt; s_t or c_t are the striction or the expansion in radial and/or axial directions; and h_t is the length of the deformed zone of the belt. In Fig. 17 is reported a scheme of tensioning error of a layer.
When there is a striction for excessive tensioning coordinates a_{ts} and b_{ts}, that identify position of the error, are given by following expressions

$$a_{ts} = r + 0{,}5 (h - s_t) \quad (19)$$

$$b_{ts} = 0. \quad (20)$$

When there is an expansion for low tensioning the coordinates are given by

$$a_{tc} = r + 0{,}5 c_t \quad (21)$$

$$b_{tc} = 0. \quad (22)$$

Referring to Fig. 18, the local spreading error gives an unbalance that can be expressed analytically as an unbalancing mass Δm_t. In case of perimetral defect this is given by

$$\Delta m_{tp} = \rho L L_t d_t. \quad (23)$$

In case of axial defect it is given by

$$\Delta m_{tp} = \rho L L_t d_t \quad (24)$$

where ρ is the density of the defective layer; h represents thickness of the layer; L_t is the axial or radial dimension of a portion of a layer that is interested by the defect; and d_t is the dimension of the defect. In Fig. 18 is reported a scheme of spreading defect of a layer.
The centre of mass is identified by coordinates a_t and b_t, whose expressions are in the case of perimeter defect in the form

$$a_{tp} = r + 0{,}5 d_t \quad (25)$$

$$b_{tp} = 0 \quad (26)$$

and in case of axial defect in the form

$$a_{ta} = r + 0{,}5 h \quad (27)$$

$$b_{ta} = d_d + 0{,}5 d_t. \quad (28)$$

Referring to Fig. 19, the shift error of layers gives an unbalance that can be expressed analytically as an unbalancing mass Δm_e. In case of localized error in a perimetral extension L_e it is given by

$$\Delta m_e = \rho h L_e e_d \quad (29)$$

where e_d represent the dimension of the shift error of the layer. In case of error extended for all perimeter extension, L_e is equal to 2π r. In Fig. 19 is reported a scheme of the shift error.

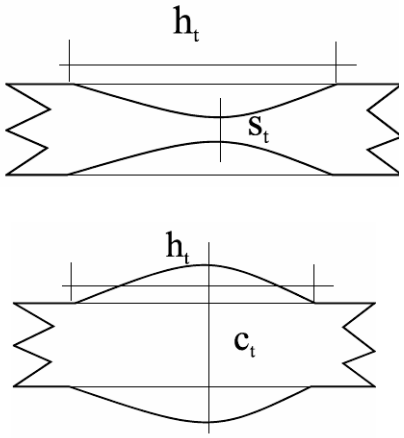

Figure 17 A scheme and parameters of tensioning error of a layer (s_t or c_t: striction or expansion in radial and/or axial directions; h_t: length of the deformed zone of the layer).

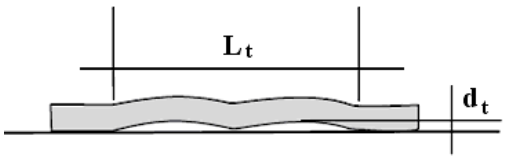

Figure 18 A scheme and parameters of spreading defect of a layer (L_t: axial or radial dimension of portion of the layer interested; d_t: defect dimension).

The centre of mass is identified by coordinates a_{el} and b_{el} that are given by following expressions

$$a_e = r - 0{,}5 h \quad (30)$$

$$b_e = 0. \quad (31)$$

Referring to Fig. 20, the deposition error of a belt gives an unbalance that can be expressed analytically as an unbalancing mass Δm_{dc}, given by

$$\Delta m_{dc} = \rho s_{dc} h L. \quad (32)$$

The centre of mass is identified by coordinates a_{dc} and b_{dc} that are given by following expressions

$$a_{dc} = r + 0{,}5\ L_c \sin \alpha_c \quad (33)$$

$$b_{dc} = d_c + 0{,}5\ L_c\ (1- \cos \alpha_c) \quad (34)$$

where s_{dc} is the length of the defective area, L_c is the width of the layer and α_c angle of deposition error. In Fig. 20 is reported a scheme of deposition error of a layer.

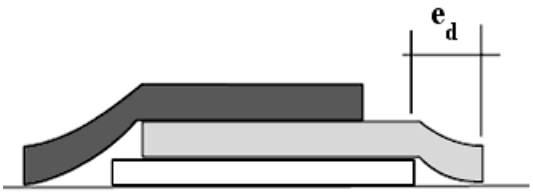

Figure 19 A scheme and parameters of the shift error (e_d: shift of the layer).

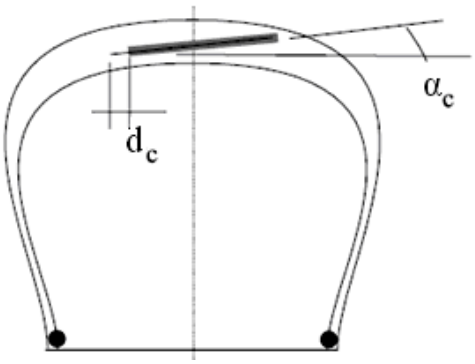

Figure 20 Scheme and parameters of deposition error of a layer (α_c: angle of deposition error, d_c: shift of the layer).

Referring to Fig. 21, the error of centering in layer deposition gives an unbalance that can be expressed analytically as an unbalancing mass Δm_{com}, given by

$$\Delta m_{com} = \rho\ s_{com}\ h\ L. \quad (35)$$

The centre of mass is identified by coordinates a_{com} and b_{com} that are given by following expressions

$$a_{dc} = 0 \quad (36)$$

$$b_{dc} = e_{com} \quad (37)$$

where s_{com} is the length of the defective area and e_{com} is the parameter for the distance between center of mass and correct centered position. In Fig. 21 is reported a scheme of centering defect of a layer.
In Figs. 22 and 23 additional indicative models are represented by means of lumped parameters. This analysis can be used to determine the influence of each mentioned source or of data of experimental test in a study of dynamic response of a tyre. The schemes in Fig. 22 refer a correct assembly of a tyre united but with a deformed configuration. This case can be modeled with proposed formulations by using a reference angle to describe tyre deformation.
A model that can be used for a physical interpretation of experimental data of dynamic response is shown in Fig. 23. The model gives the identification of concentrated parameters (of compliance and damping related to lumped masses) and/or of distribution of the components to differentiated dynamic behaviors.

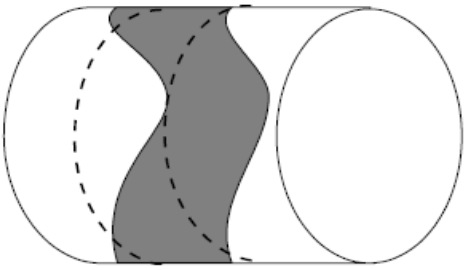

Figure 21 A scheme of centering defect of a layer.

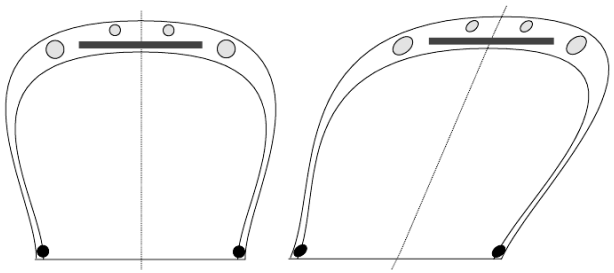

Figure 22 A scheme for an analysis of weight distribution in a semi-section of a tyre: (a) symmetric geometry; (b) skew structural configuration.

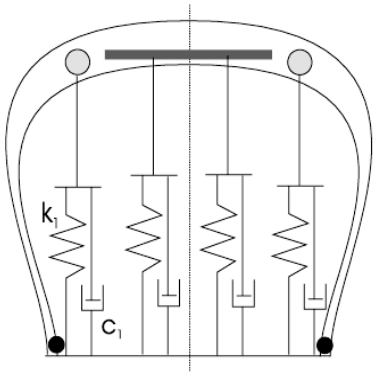

Figure 23 A scheme for a structural characterization trough lumped parameters in a tyre model.

6 A PROCEDURE FOR AN EXPERIMENTAL EVALUTATION

Experimental tests can be used to validate the proposed models and to characterize possible balance errors. A guideline is outlined to identify main steps and parameters

of interest for an experimental procedure as in the following:

1) Definition of design characteristics for a specific unbalance source;
2) Construction of a tyre with an exaggerated unbalance due to defined sources;
3) Tests with built tyres to measure unbalance errors;
4) Interpretation of results.

Design characteristics of tyres for experimental tests are chosen to make evident the influence of unbalance sources. Then these are implemented on the manufacturing machine and tyres are built.

Unbalance measures are obtained by using Model AIT Tyre Dynamic Balance System of Micro-Poise Measurement Systems at Marangoni Tyre plant in Anagni, as shown in Fig.24.

A measure is obtained by locating a tyre in within measure tools, inflating air into the tyre and rotating tools, as shown in Fig. 25. An unbalance measure of tyres is based on the theory of centrifugal forces. A weight (m) in rotation with a constant angular velocity (ω) at distance (r) from the rotation axis will generate a force along radial direction given by

$$F=m\omega^2 r \tag{38}$$

Static and couple unbalances generate two forces in the planes of the tyre, respectively as shown in Fig. 26 (a) and (b). In Fig. 26 are also shown the sinusoidal variation of reactions forces by two fixed mass points.

The Model AIT Tyre Dynamic Balance System uses two load cell sensors that are located in the measure tools in order to evaluate reaction forces during rotation of an unbalanced tyre. Then, the machine displays in a monitor the amount and position of the unbalance mass in the tyre. These values are then used to verify the congruence with expected results from the above as mentioned models and numerical formulation.

Figure 24 The Model AIT Tyre Dynamic Balance System (courtesy of Marangoni Tyre S.p.A).

(a)

(b)

Figure 25 Three steps of measure operation by the Model AIT Tyre Dynamic Balance System: (a) locating a tyre on measure tools; (b) inflating air into the tyre; (c) rotating tools to measure unbalance values (courtesy of Marangoni Tyre S.p.A).

7 RESULTS OF NUMERICAL EXAMPLES AND OF AN EXPERIMENTAL TEST

The effect of sources of unbalance that are shown in Figs. from 14 to 21 can be evaluated numerically by using the proposed expressions in equations from (5) to (37). An example of numerical results is reported in Table I. The width of the layer is considered L=195mm, the radial size of the tyre r=307 mm and the density ρ=1.2 g/l. In addiction, experimental tests have been carried out as referring to specify unbalance sources.

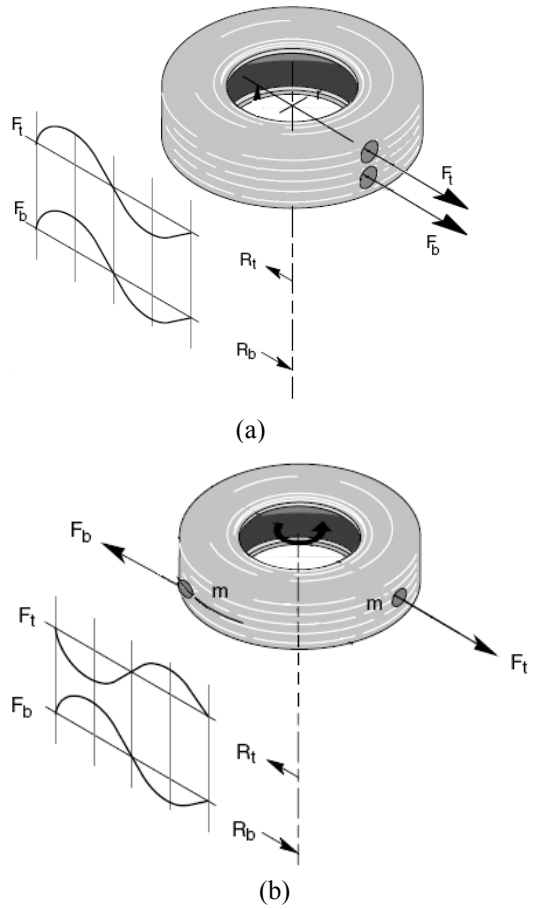

Figure 26 Schemes for forces and trend of reaction forces that are generated during rotation of: (a) a static unbalanced tyre; (b) a couple unbalanced tyre [1].

Table I - Illustrative values of unbalance errors as referred to models from Fig. 14 to 21 with L=195 mm, r=307 mm and ρ=1.2 g/l.

Unbalance sources	**Fig.**	**Size of unbalance source [mm] and [°]**	**Unbalance mass [g]**	**Radial coord. [mm]**	**Axial coord. [mm]**
Overlap of junction	Fig.14	h=1.2; s_L=10; t_L=5; d_L=1.	1.46	307.6	87.45
Junction error	Fig.15	ρ_G=ρ; s_G=0.8;d_G=0.1.	0.156	307.6	97.6
Local error	Fig.16	L_d=10; s_d=10; d_d=10.	0.1	307.5	15
Tensioning error	Fig.17	h_t=50; s_t=1.0	9.75	307	0
Extending defect	Fig.18	L_t=100; d_t=0.1.	1.95	307.05	0
Shift error	Fig.19	L_e=100; e_d=10.	1	306.5	0
Deposition error	Fig.20	L_c=200; α_c=10/180π; d_c=1; s_{dc}=25; h=1.2.	7	334.36	2.52
Centering defect	Fig.21	e_{com}= 10; s_{com}=25; h=1.2.	7	307	10

An experimental test has been carried out as referring to a tyre where tread has more than 25% of the total weight. The overlap of the edges junction, the tensioning error and their interactions have been analyzed by referring to the tread layer of a tyre model as Marangoni Verso 195/60R15.
The overlap area of a junction is obtained by over-sizing the dimension of the belt of tread with a length value S_L. The tensioning error of the layer is given by a striction S_T, as shown in Fig. 17, as generated during the rolling of the reel. This can be limited by imposing elevate stretching pressure (P_M) on the multiroller of the green tyre building machine, as shown in Fig. 27. The pressure of the multiroller is used to couple layers and can generate an expansion C_T, as shown in Fig. 17.
Characteristics of the tests are reported in table II. Maximum overlap of the edges in the junction (S_t=20 mm) and maximum pressure of the multiroller (P_M=20 bar) are indicated with 1. Minimum values (S_t=0 mm) and (P_M=0 bar) are indicated with 0. In table III data for the test are reported referring to dimensions of the tread belt shown in Fig. 28. These values have been measured after the cut by tread belt from the continuous beam and before the assembly of the green tyre.
In table IV results are reported as mean unbalanced values measured with built tyres. In particular, the following can be observed. The imposed error of overlap area of the tread layer gives an increase of static unbalance value (see values of tests 2 and 4) with respect to others with no overlap area (see values of tests 1 and 3). Maximum pressure due to multiroller limits the effect of imposed error. In fact, the mean static unbalance value of tyres of the test 4 is smaller than the value of the test 2. In addiction, the values of mean static unbalance of tyres with no imposed balance errors are similar (see values of tests 1 and 3). Thus the effect of manufacturing errors can be limited by using maximum pressure with multiroller. This can be explained as a homogeneous distribution of materials in a tyre. As expected the mean couple unbalance values of tyres in tests are similar. In fact, errors examined are symmetric with respect to equatorial plane of a tyre and therefore they generate only static unbalance.

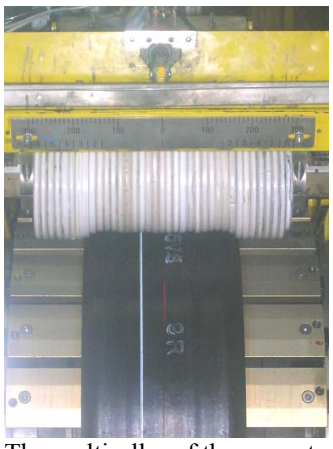

Figure 27 The multiroller of the green tyre building machine (courtesy of Marangoni Tyre S.p.A).

Table II - Characteristics of built tyres for experimental tests.

n° test	Pressure of the multiroller	Overlap of the junction of edges
1	0	0
2	0	1
3	1	0
4	1	1

Table III - Parameter data for experimental tests with tyre of table II.

n° test	1	2	3	4
L_B [mm]	192	192	190	192
M [mm]	1820	1832	1810	1836
h_{max} [mm]	7.3	7.15	7.1	7.25
h_{min} [mm]	6.25	6.15	6.2	6.2
weight [kg]	2.772	2.686	2.612	2.744
S_t [mm]	192	190	189	192

Table IV - Results of experimental tests with tyre in table II.

N° test	Upper counterbalance mean value [g]	Lower counterbalance mean value [g]	Static unbalance mean value [g]	Couple unbalance mean value [g]
1	13.64	19.49	26.78	10.18
2	32.31	36.61	66.71	11.00
3	13.08	22.32	29.07	11.37
4	16.98	30.94	43.25	12.77

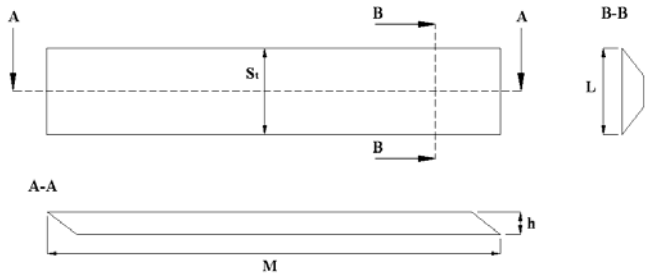

Figure 28 A scheme of main dimensional parameters of a tread layer.

8 CONCLUSIONS

This paper has addressed the attention to the problem of unbalancing of pneumatic tyres. Main sources of unbalance have been identified by referring to a standard production process. Mathematical models have been proposed in order to provide a quantitative measure of the contribution of each unbalance source in a pneumatic tyre. A procedure for experimental tests has been proposed by referring to a commercial tyre dynamic balance measuring system. Preliminary experimental tests have been reported to show the effectiveness of the proposed analysis and to propose how to evaluate and to characterize experimentally balance errors in tyres.

ACKNOWLEDGEMENTS

The second author wishes to thank Marangoni Tyre S.p.A. in Anagni, Italy, for a grant that has permitted him to spend three months in the production line and testing laboratory of Marangoni plant.

REFERENCES

[1] AIT_WIN, ITW Micro Poise, *Model AIT, Dynamic Tire Balance System Windows_Operating System*. Akron, Ohio USA, 2005, pp. 3.1-3.9.

[2] Dimiccoli D., Main technical characteristics of tyres. *Auto Tecnica, Nuovi Periodici Milanesi*, Milano, 1997, pp. 86-95.

[3] Garrett T.K., Newton K., Steeds W., *The Motor Vehicle*. Butterworth and Heinemann, Woburn.

[4] Genta G, *Mechanics of vehicles*. Levrotto & Bella, Torino, 2000, pp. 37-38.

[5] Longhurst C., *The wheel and tyre bible*. http://www.carbibles.com/tyre_bible.html, 2007.

[6] Rivolta, *Balance weights with no lead*. Catalogue 2007, http://212.97.41.154/ita/rivolta_spa/Catalogo/pagine_auto/pag.%2048-60.pdf.

[7] Wilson D., *How a tyre is made*. http://www.tyres-online.co.uk/techinfo/howmade.asp, 2007.

[8] Zagatti E., Zennaro R. and Pasqualetto P., *Vehicle configuration*. Levrotto & Bella, Torino, 1998, pp. 65-105.

ISSN 1590-8844
International Journal of Mechanics and Control, Vol. 11, No. 02, 2010

PRINCIPAL SERVOCONTROLLER FAILURE MODES AND EFFECTS ON ACTIVE FLUTTER SUPPRESSION

Lorenzo Borello* Giuseppe Villero* Matteo Dalla Vedova*

* Department of Aerospace Engineering, Politecnico di Torino, Turin, Italy

ABSTRACT

Conventional active flutter and vibration control technology relies on the use of aerodynamic control surfaces operated by servo-hydraulic actuators, which can be affected by some specific types of failure. In order to assure a sufficiently high safety degree, it is necessary to verify the dynamic behaviour of the whole system when a defined failure occurs. The purpose of this paper is to analyze the aeroservoelastic behaviour of a typical wing with active flutter suppression performed by a hydraulic servomechanism equipped with a defined proper control law (relating the required surface deflection angle to speeds and acceleration of the main aerofoil surface) and affected by the principal modes of servocontroller failures. Active control and its failure modes have been implemented within the model of a representative actuation system acting on a wing structure embedded in a defined aerodynamic field.

Keywords: Failure, flutter, flight controls, active suppression.

1 INTRODUCTION

Aeroelasticity is the mutual interaction between deformations of the elastic structure and aerodynamic forces induced by the structure deformations. Combined, these effects may cause an aircraft structure to become unstable above a defined value of flight speed. If the interaction between deformations and aerodynamic forces involves also the inertia, the phenomenon, called flutter, is an oscillatory instability that occurs when the structural damping transitions from positive to negative due to the presence of aerodynamic forces. During this transition, two modes of vibration coalesce to the same frequency and achieve an aeroelastic resonance. Bending and torsion are the two most common vibration modes of a wing which coalesce to flutter. In modern aircrafts the use of automatic flight control systems with powered control surfaces has further complicated the problem.

Contact author: Borello[1], Villero[2], Dalla Vedova[3]

[1] lorenzo.borello@polito
[2] giuseppe.villero@polito
[3] matteo.dallavedova@polito.it
Corso Duca degli Abruzzi 24 – 10129 TORINO

This interaction between structural dynamics, unsteady aerodynamics and the flight control system of the aircraft, known as aeroservoelasticity, has been and continues to be an extremely important consideration in many aircraft designs. To prevent undesirable aeroelastic effects, the stiffness of the wing must be increased, adding weight to the aircraft and decreasing the overall performance: this approach is known as "passive control". A recent alternative to passive control is the so called "active control" through feedback to control surfaces (conventional technique), or, more recently, through feedback to active materials. These vibration control technologies allow flight vehicles to operate beyond the traditional flutter boundaries, improve ride qualities, and minimize vibration fatigue damage. Many control strategies have been applied to suppress flutter or to control unacceptable wing motion. Conventional active flutter and vibration control technology relies on the use of aerodynamic control surfaces operated by servo-hydraulic actuators. In this conventional configuration the flutter and vibration suppression algorithms are implemented through the servovalve/hydraulic actuator, capable of producing (if necessary in presence of large oscillation amplitude) large forces and large surface displacement, but having some limitations, such as limited actuation speed in saturation conditions and limited frequency range. In contrast, active materials technologies offer high-frequency responses but

their typical shortcomings are limited forces and displacements performed.
Generally, these problems have been already studied by several authors, but no work specifically concerns the effects on the aeroelastic system of the most important failure modes affecting the flutter servocontroller, as:

- servovalve feedback spring failure
- hydraulic system pressure drop
- whole active flutter control failure
- piston seizure
- piston internal sealing failure.

The aim of this paper is the analysis of the aeroservoelastic behaviour of a typical wing with active flutter suppression performed, through a defined control law, by a fly-by-wire hydraulic servomechanism affected by the aforesaid modes of servocontroller failures.

2 DESCRIPTION OF AEROSERVOELASTIC MODEL

Figure 1 shows the typical wing section that is used to derive the structural equations of motion. The two degrees of freedom associated with the aerofoil motions are the vertical displacement h and the pitching displacement θ.
The displacements are restrained by a pair of springs attached to the elastic axis with linear spring constants K_θ and K_h and cubic one $K_{\theta c}$ and K_{hc} respectively. The airfoil is equipped with a trailing edge moving surface, whose position δ depends exclusively on the servomechanism position and is not affected by the aerodynamic and inertial loads. The servomechanism position depends, through its dynamic model, on the output of an adequate flutter suppression control law. The aerodynamic model computes lift and pitch moment related to the aerodynamic centre as a function of the dynamic pressure, the initial value of the angle of attack α, the pitching displacement θ, the vertical and pitching rates and the surface deflection angle δ.

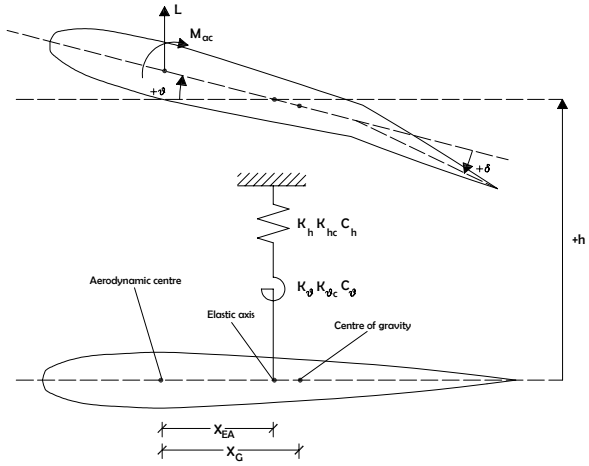

Figure 1 Aeroelastic parameter definition.

The structural dynamic model computes vertical and pitching accelerations related to the elastic axis as a function of aerodynamic loads L and M_{ac}, inertial loads, weight, structural damping and stiffness. The structural damping is considered as a linear function of the speed, while the structural stiffness is modelled as a linear and cubic function of the displacement. The sign of the cubic coefficient takes into account the softening or hardening effects. The actuation system of the aerodynamic surfaces consists of a Power Control and Drive Unit (PDU, equipped with position transducers and tachometers), directly connected to the lever arm of the surfaces. The system control is performed by an Electronic Control Unit (ECU), which closes the position control loop. The PDU contains the hydraulic jack and the control valve.

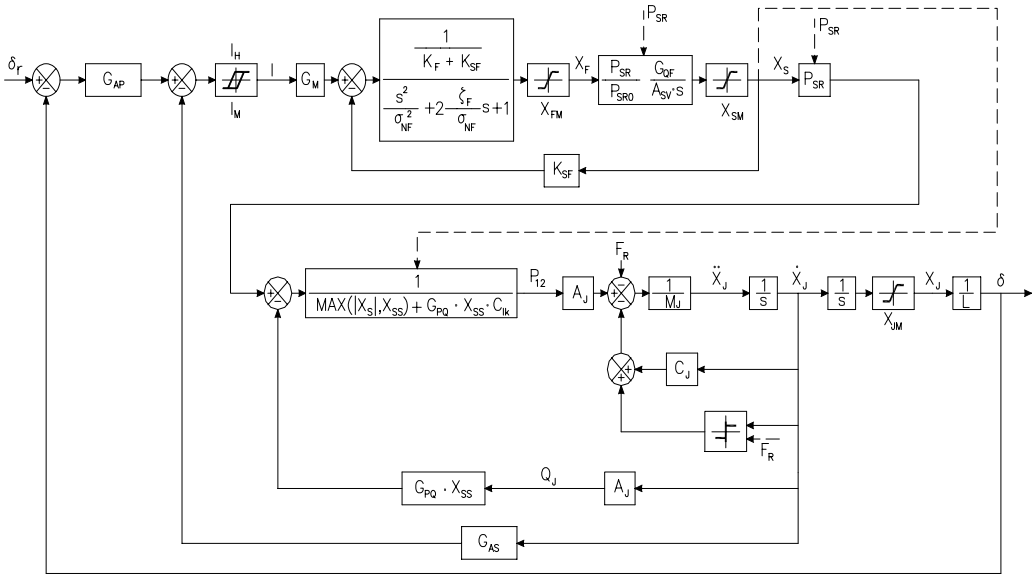

Figure 2 Block diagram of the model of the actuation system.

The model of the actuation system, as reported in figure 2, takes into account the hydraulic and mechanical characteristics of all system components as follows:

- Coulomb friction in the PDU-surface assembly;
- third order electromechanical dynamic model of the servovalve with first and second stage ends of travel;
- fluid-dynamic model of the servovalve taking into account the maximum differential pressure, eventually time varying, performed by the hydraulic system1;
- dynamic and fluid-dynamic of hydraulic jack taking into account, beside the above mentioned Coulomb friction, viscous friction and internal leakage.

The high complexity of the actuation system servomechanism model is requested by the necessity of taking into account the effects of the above mentioned several nonlinearities on the effectiveness of the flutter suppression active control.

Active control has been implemented within the proposed model, in order to investigate active means of flutter suppression via control surface motion. A simple control law is used which relates the required surface deflection angle δ_r to the speed and the acceleration of the main aerofoil surface (heave and pitch degrees of freedom). Hence, δ_r is evaluated according to the following equation:

$$\delta_r = G_{h2}\ddot{h} + G_{h1}\dot{h} + G_{\vartheta 2}\ddot{\vartheta} + G_{\vartheta 1}\dot{\vartheta} \qquad (1)$$

where the G's are the gains of the system.

3 SYSTEM COMPUTATIONAL MODELLING AND RESULTS

The above described models have been used to build a mathematical model of the whole system and a dedicated computer code has been prepared. A structural model having linear and cubic softening spring characteristics around the pitch axis and linear along the vertical displacement is considered. The aerodynamic model is described as linear and the considered flight speed is slightly greater than the critical flutter speed.

Some simulations have been run in different failure conditions, in order to verify the criticality of the actuation system failures on the flutter suppression active control. All the following figures show the behavior of the system in terms of vertical displacement h and pitching angular displacement θ: their trend is typically oscillatory, characterized by a frequency slightly depending on the corresponding amplitude, having an average value of approximately 14,5 Hz. The curves reported in the figures represent the envelopes of the eventually damped oscillations.

Figure 3 shows the behaviour of the system characterized by a fully operational (no failures) active flutter control, in terms of vertical displacement h and pitching angular displacement θ, employing the control law (1) applying a not null value only to the gain $G_{\theta 2}$, because this is a satisfying solution as discussed in [1].

In this case the slow growth of the oscillations amplitude, following the application of a large step perturbation concerning the pitching displacement at time t = 1 s, is suppressed by the active flutter control.

This case must be considered as reference condition for the following simulations.

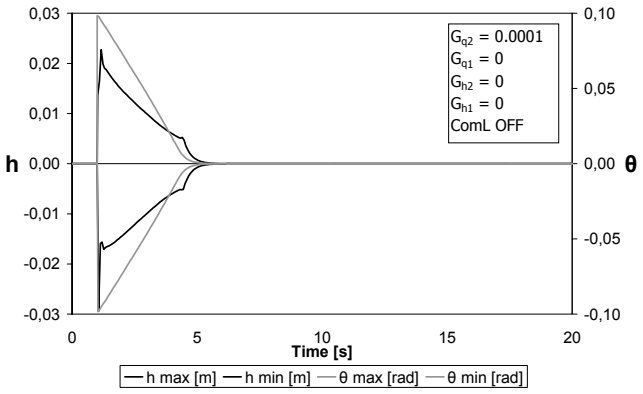

Figure 3 Fully operational system.

Figure 4 shows the dynamic behaviour of the system in the servovalve feedback spring failure condition. The failure occurs at time t = 2 s. With respect to Figure 3, the behaviour is substantially identical as long as the amplitude of the servomechanism input command is so large to produce end of travel displacements of the servovalve spool, because in this condition the feedback spring is practically ineffective. Some small differences are detectable when the amplitude of the input command is substantially reduced and the ends of travel are no longer important in the displacement of the servovalve mechanical elements. However the servomechanism, though affected by a limit cycle giving rise to fatigue damage, is able to perform a response on average close to the commanded position. In fact the limit cycle frequency is higher than any structural frequency, so its effect is marginal for the aeroelastic phenomenon.

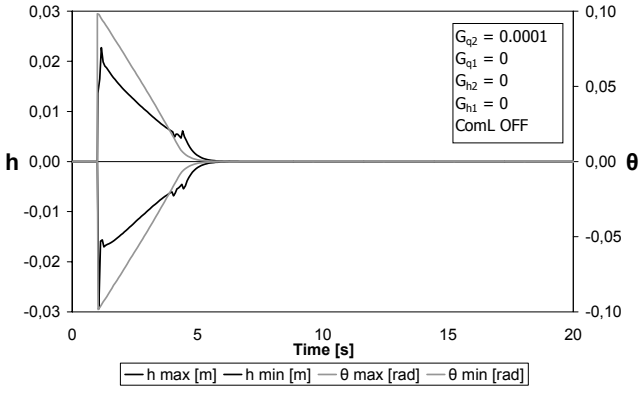

Figure 4 Feedback spring failure.

Figure 5 shows the dynamic behaviour of the system in

case of hydraulic system pressure drop to a very low value (1 MPa) occurred at time t = 2 s, when both the servovalve spool and the moving surface are far from the centered position. The available actuation speed at a very low pressure value is very small, so the moving surface should no longer be able to retract to the null position. In this case the surface is progressively driven, through a series of oscillations, to the null position mainly by the aerodynamic load, overcoming the supply pressure effect. However the reduced available actuation rate prevents an effective flutter corrective action.

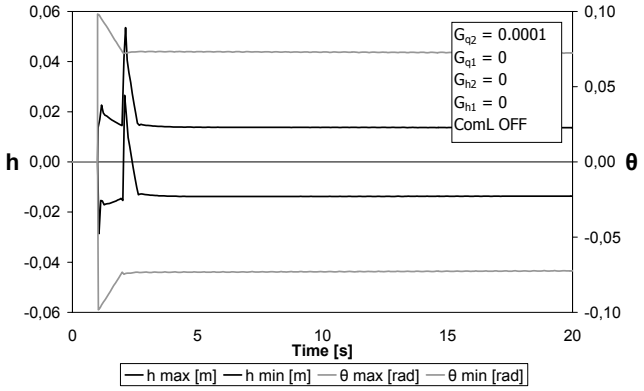

Figure 5 Hydraulic pressure drop to a very low value.

Figure 6 shows the dynamic behaviour of the system in case of hydraulic system pressure drop to a higher value than the previous case (5 MPa) occurred at time t = 2 s. The available actuation rate is higher than in Figure 5, so the flutter corrective action is slightly more effective.

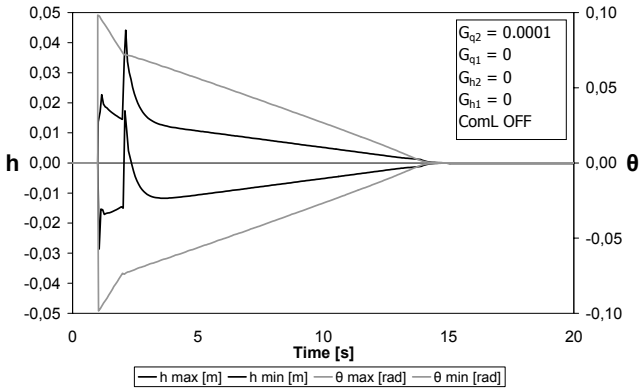

Figure 6 Hydraulic pressure drop to a higher value than the previous case.

Figure 7 shows the same pressure drop of Figure 5 at time t = 2 s, then followed by a pressure restore to the normal value (20 MPa) at time t = 5 s. As expected, it can be noted, till to 5 s, the same behaviour reported in Figure 5. At the pressure restore the corrective ability of the servomechanism is now fully available, and the behaviour of the system is similar to Figure 3.

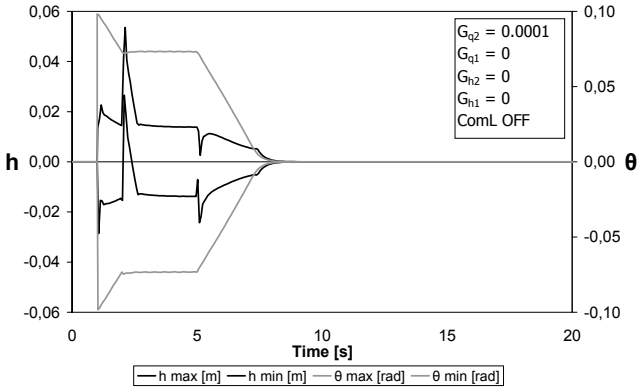

Figure 7 Hydraulic pressure drop and subsequent restore.

Figure 8 shows the dynamic behaviour of the system in case of whole active flutter control failure, intended as the loss of the servomechanism input command (constantly null), without any failure strictly regarding the servomechanism integrity. When the failure occurs, the surface is quickly retracted to the null position, remaining ineffective through the following part of the simulation. As expected, the flutter phenomenon is slightly divergent, as in case of absence of active flutter control.

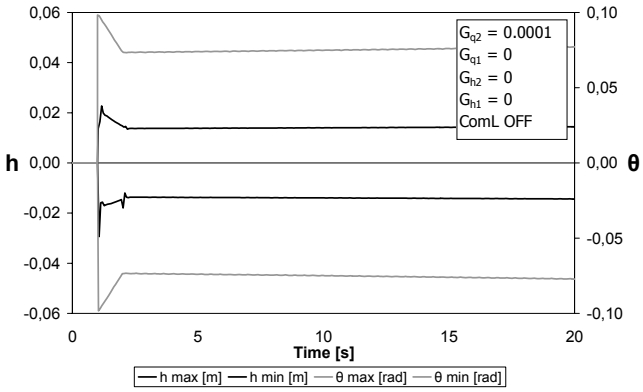

Figure 8 Whole active flutter control failure.

Figure 9 shows the dynamic behaviour of the system in case of incipient piston seizure, modelled as a marked rise of the friction force to a value slightly lower then the stall piston one. As a consequence, the servocontrol actuation rate, still possible, is however lower than usual, so the corrective capability is reduced.

Figure 10 shows the dynamic behaviour of the system in case of piston seizure, modelled as a more marked rise of the friction force to a value higher then the stall piston one. When the failure occurs, the surface is stopped in a position far from the centered one, and its flutter corrective action is lost. More, the not null surface position is able to keep the wing structure in a deformed position, as it is evident

mainly in terms of vertical displacement.

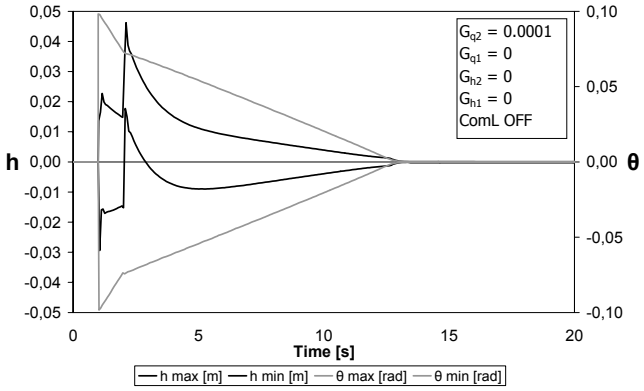

Figure 9 Incipient piston seizure.

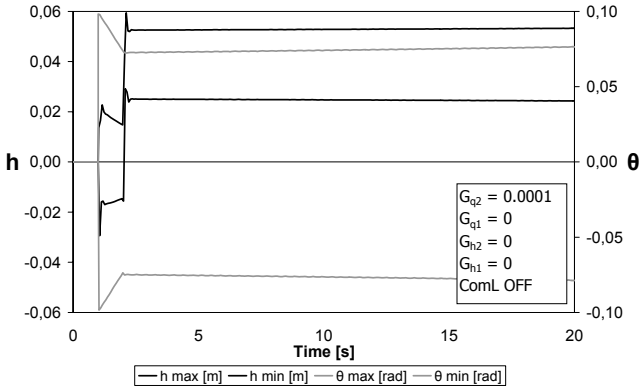

Figure 10 Piston seizure.

Figure 11 shows the dynamic behaviour of the system in case of marginal piston internal sealing failure, modelled as a medium growth of its leakage coefficient. Under low to medium aerodynamic loads, the actuation capability is slightly reduced (lower rate) but substantially preserved. As a consequence the flutter corrective action is slightly lower than the case shown in Fig. 3.

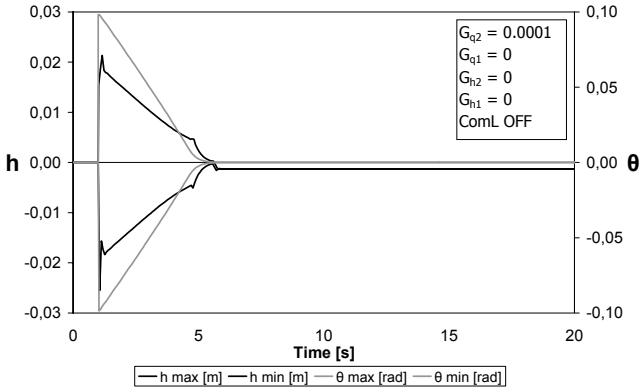

Figure 11 Marginal piston internal sealing failure.

Figure 12 shows the dynamic behaviour of the system in case of piston internal sealing failure, modelled as a large increase of its leakage coefficient. In this case the actuation capability is markedly reduced even under low aerodynamic loads. On the contrary the aerodynamic load is often able to overcome the input command and the surface deployment is mainly the consequence of the load itself. This effect produces a negative corrective action, so developing higher divergence rate.

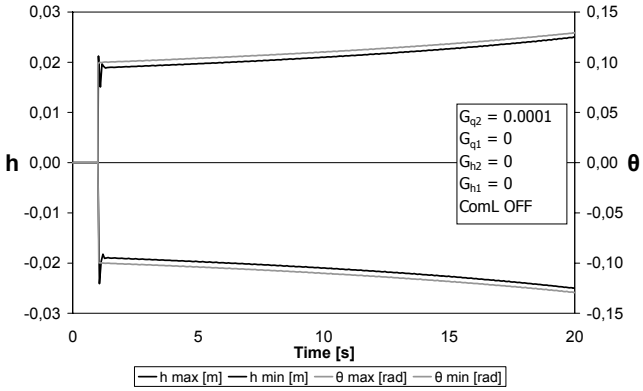

Figure 12 Piston internal sealing failure.

4 CONCLUSIONS

The results presented in this work are obtained in case of not redundant servosystem; so the failure effects are not limited by the action of the operative portion of an eventually redundant device. However the results are significant mainly for their conceptual aspects and show the possible criticality of a singular failure in a not redundant device. It can be noted that the more critical failures are those concerning the loss of the piston internal sealing, the total supply pressure drop or the total piston seizure. Sealing damage and pressure drop can be efficiently overcome by a proper redundancy; on the contrary, the piston seizure, particularly in case of force summed redundancies, must be considered seriously critical because the operative portion of the system may be incapable of overcoming the failure effects.

REFERENCES

[1] Borello L., Villero G. and Dalla Vedova M., 2008. Effects of nonlinearities and control law selection on active flutter suppression. *International Journal of Mechanics and Control,* Vol. 9, No. 1, pp. 27-39.

ISSN 1590-8844
International Journal of Mechanics and Control, Vol. 11, No. 02, 2010

EVALUATION OF FEASIBILITY OF MECHANICAL HARVESTING OF MYRTLE BERRIES (*Myrtus communis L.*)

F. Gambella F. Paschino

Department of Agricultural Engineering, University of Sassari, Viale Italia 39, 07100 Sassari, Italy

ABSTRACT

The use of machinery for the mechanical harvesting of small fruits requires a detailed study of the physical characteristics of the fruits. In this work the parameters (mean geometric diameter, fruit surface area and apparent elasticity) to be considered for the purpose of designing mechanical systems for use in the harvesting and interception of myrtle berries are defined. Three different varieties grown were compared: RUM 4 was found to be the most suitable for harvesting with facilitating machinery.

Keywords: myrtle berries, myrtle leaf, test compression, air rate, mechanical harvest.

1 INTRODUCTION

Myrtle, *Myrtus communis L.*, is a steno-Mediterranean frutescent species that grows spontaneously in Italy, Spain, France, Tunisia, Algeria and Morocco (Figure 1). In Italy, it is present in almost all coastal areas and mainly on the islands. The myrtle is a shrub averaging 1,5 m, but grooving up to 2,5 m in height [1], [2].

Figure 1 The myrtle plant (*Myrtus connunis L*)

Contact author: Filippo Gambella[1], Francesco Paschino

Department of Agricultural Engineering, University of Sassari, Viale Italia 39, 07100 Sassari, Italy
phone: +39 079 229281 – fax: +39 079 229285
Email: [1] gambella@uniss.it

The myrtle fruit is a spherical or ellipsoidal berry whose colour varies from red to deep purple and white. In Sardinia, the berries are the raw material used in the making of red and white myrtle liqueur [3], [4]. The market for this product is in a period of strong expansion: in Sardinia in the ten-year period from 1995 to 2005 the production of red myrtle liqueur increased by 173.5%, with a production of 1,574,730 litres/yr, corresponding to 276,657 kg/yr of harvested berries. The fresh product is harvested by hand by rakes, prevalently from spontaneous plants, with a noteworthy expenditure of manpower [5]. Mechanical harvesting is still primarily limited to fruit be processed. Although some producers have successfully marketed mechanically harvested fruit in the fresh market, current harvesting and handling techniques generally cause too much fruit damage for the fresh market. The declining availability and rising cost of agricultural labour will pressure myrtle producers to mechanize production and handling practices even further. A major obstacle to further mechanization appear to be loss in small berries quality associated with traditional harvester[6], [7]. Dale *et alt* described continuou harvester prototype developed by ARS, USDA engineers, Michigan State University, which have “fingers” of steel that can detached over 90% of mature blueberry, along with some green fruit an leaves. At last Dale describes other harvester that have good potential for the picking mechanism but produce always damage in the mature blueberries which have similar dimension of the myrtle berries [8]. On the basis of these considerations, the modification of an equipment was arranged for picking olives, in one able to strike also the myrtle berries. The modifications produce, were the inter- axe space reduction

between “fingers” and the protection of the same ones with a sheath in silicon to reduce any damage from contact among “fingers” and fruit. The manual harvester with an rotating mechanisms was designed for low bushes or small plants (Figure 2).

Figure 2 Equipment utilized for the harvest of myrtle berries producted by COIMA-(Italy)

These appear to be more delicate and less aggressive respect the traditional “finger” harvester. If protected may reduce berry damage, consequently, a detailed study of the fruit’s physical characteristics (diameter, sphericity, surface area, weight and real and apparent volume) and mechanical movement of small harvesting systems and fruits damage was carried out to define the relationships between machine and fruit [8], [9], [10], [11]. Shape, size, volume, surface area, density, porosity, colour and appeareance are some of the physical characteristics which are important in many problems associated with design of specific machine or analysis of the behavior of the product in handling of the material.

2 AIM OF THE WORK

The aim of the work is to evaluate response of three autochthonous myrtle berries varieties and their adaptability for mechanical harvesting by an electric comb with protected “fingers”. The second obiective was carried out a detailed study of the fruit’s physical characteristics (diameter, sphericity, surface area, weight and real and apparent volume) and the relationships between mechanical movement of small harvesting systems and fruits damage.

3 MATERIALS AND METHODS

The use of this mechanical systems provides evident advantages in increasing production, respect to the hand picking, but they can also cause damage to the product through contact with both branches and berries, especially the latter, whose integrity is fundamental for obtaining a high-quality liqueur product. For this reason the “fingers”, made in titanium, was protected by silicon sheaths having a thickness of 0.5 mm. It is perfectly clear that the action of the non protected combs on the berries may cause some damage to the fruits and consequently compromise the integrity of the product which have shape and size bigger than the distance between “finger” (15,5 mm) because the berry through comes its and sustained a damage more o less severe. Then, the dimensional parameters of the berries must be measured. These, were measured on a sample of 100 berries with three replications, picked randomly; the parameters determined were: longitudinal (L), transversal (T) and intermediate (W) diameters means by an electronic callipers, model S 225 (Wurth) with a resolution of ± 0,001mm; the mean geometric diameter (Dg); sphericity (Φ) expressed as a percentage and berry surface area (S) calculated using the Mohsenin (1), (2) and Baryeh (3) formulas [12], [13]:

$$Dg = (LWT)^{1/3} \quad \text{(Mohsenin, 1970)} \quad (1)$$

$$\Phi = \frac{(LWT)^{1/3}}{L} 100 \quad \text{(Mohsenin, 1970)} \quad (2)$$

$$S = \pi \ Dg^{2} \quad \text{(Bryeh, 2001)} \quad (3)$$

The average weight (P) of 100 berries expressed in grams was determined by means of a digital scale, model Mettler PC 180 with a resolution of ± 0.001g for determine the percentage of weight class distribution that form the population of the berries during the harvest. Normally, the mechanical damage in agricultural products are due either to external forces under static and dynamic conditions or internal forces. At last, in order to evaluate berry dimension during the harvest, if the contact with the teeth of the electrical comb was producing a some modification of the product picked up in terms of damage or in terms of modify the form we calculated the apparent modulus of elasticity (Ea) in kPa/mm2, using a motorized stand (LF-Plus) and following the ASAE S 368.3 standard (4) [14] for spherical berries submitted to uniaxial compression by means of a single contact plate. The detachment force was measured by an portable digital force gauge (IMADA) on a sample of 100 berries with three replications, picked randomly. As concerns the leaves, in both experimental plots the same biometric parameters of the berries the air rate (Vt), were determined as well as using an air separator created for the purpose, while air rate was measured by means of a hot-wire anemometer (model DO 2003, HVACR, produced by Delta OHM), (Figure 3).

3.1 Apparent Modulus of Elasticity (AME)

The AME of the myrtle berries was calculated using equation 4 of the ASAE S368.4 Dec.2003 for parallel contact plate

$$E = \frac{0.338\ F((1-\mu 2)}{D\frac{3}{2}}\left[KU + \left(\frac{1}{RU}+\frac{1}{R'U}\right)1/3\ KL\left(\frac{1}{RL}+\frac{1}{R'U}\right)1/3 -\right]1/3 \quad (4)$$

where:

E = apparent modulus of elasticity (N/m ^{2})
D = deformation (mm)
F = force in Newton (N)
μ = Poisson's ratio (dimensionless)
R_U and R'_U = radii of curvature of the convex surface of the sample at the point of contact with the upper plate (mm)
R_L and R'_L = radii of curvature of the convex surface of the sample at the point of contact with the upper plate (mm)
R_U and R_L are the minimum radii of curvature of the sample at the point contact; R_L and R'_L are the maximum radii of curvature
K_U and K_L are constants.
The value of compression force needed to rupture the berries was recorded, calculated and displayed on the PC monitor at the same time using the software "Nexigen force gauge" (Loyd, Systems, version 1.0).

4 STATISTICAL ANALYSIS

The data of fruit and leaf biometric parameters, apparent elasticity and air rate were statistically analyzed using Statgraphics, XV-Centurion (StatPoint.Inc, 2005) software by means of the simple analysis of variance (ANOVA). The means, compared with the Multiple Range Test (MRT), were separated using Duncan's test (p = 0.05).

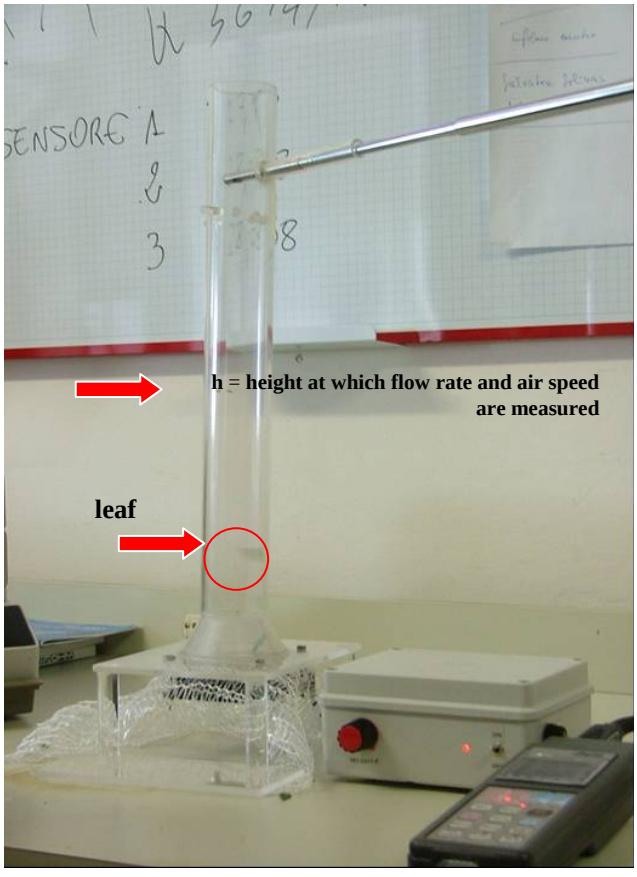

Figure 3 Air separator with speed meter model DO 2003, HVAC.

5 RESULTS AND DISCUSSION

5.1 Sizes of berries in the two experimental sites considered
In the population of the fruits analyzed at the two sites (Sella & Mosca and Pozzo d'Ussi) the distribution percentage for T and L indicate a value for T between 6.8 mm and 9.8 mm for 87.4% of the berries , while 4.6% and 8% were below 6.8 mm and above 9.8 mm respectively. Parameter T is between 6.2 mm and 8.8 mm (79%), below 6.2 mm (13%) and above 8.9 mm (8%). The mean Dg (table I) is 67% of berries between 6.8 mm and 8.7 mm, while the remaining 33% is composed of fruits with diameters either above or below this spread. Irrigation increases the Dg value of berries from the Sella & Mosca plot by 21.8%, 9.8% and by 28.6% compared to the variety grown at Pozzo d'Ussi. Seventy-five percent of the berries picked at both experimental sites had a surface area between 150 mm^2 and 240 mm^2, while the extremes were 14% (berries with S < 150 mm^2) and 11% (berries with S > 240 mm^2). The increase in surface area makes for more efficient use of mechanical harvesting besides being detached by the vibrations applied to the plant, the berries do not go through the space between the teeth of the comb and the larger size also increases the exchange surface between the berries and the water and alcohol solution.

Table I - Mean geometric diameter and surface area of berries harvested at Sella & Mosca and Pozzo d'Ussi

Parameter	Sella & Mosca (irrigated*) and Pozzo d'Ussi (not irrigated**)		
Classes	(from 5.5 mm to 6.7 mm)	(from 6.8 mm to 8.7 mm)	(from 8.8 mm to 9.9 mm)
Dg (%)*	25	67	18
Dg (%)**	15	61	14
Parameter	Sella & Mosca (irrigated*) and Pozzo d'Ussi (not irrigated**)		
Classes	(from 90 mm^2 to 130 mm^2)	(from 131 mm^2 to 240 mm^2)	(from 241 mm^2 to 300 mm^2)
S (%)*	19	75	14
S (%)**	14	67	11

The diameters L, W and T present a higher value in the irrigated fruits compared to those without irrigation (tables II and III). The Dg of the berries is, respectively, 7.63 mm for CPT 5, 8.08 mm for CPT 4 and 7.14 mm for RUM 4 harvested at Pozzo d'Ussi, while in the other experimental plot the same parameter is higher in the varieties CPT 5 and RUM 4, with 9.04 mm and 9.39 mm, and slightly lower (7.93 mm) for CPT 4. The berry surface area (S), varies from a minimum of 161.6 mm^2 for the RUM 4 variety to a maximum of 206.8 mm^2 for CPT4 harvested at Pozzo d'Ussi. The shape of the fruit is prevalently ellipsoidal, with sphericity varying from 89.8% to 79.7% at Pozzo d'Ussi and from 79.5% to 86.0% at Sella & Mosca. Concerning the site of production and the use of irrigation,

the value of *S* increases by 26.3% for CPT 5, 10.7% for CPT 4 and 21.4% for RUM 4.

Table II - Mean and standard deviation of dimensional parameters of berries of the CPT 5, CPT 4 and RUM 4 varieties harvested at Pozzo d'Ussi.

Parameter *	Unit of measurement	CPT 5		CPT 4		RUM 4	
		mean	Std. dev.	mean	Std. dev.	mean	Std. dev.
L	mm	8.44	± 0.89	9.79	± 0.80	8.14	± 0.80
W	mm	7.12	± 0.78	6.82	± 0.56	6.52	± 0.33
T	mm	7.29	± 0.96	7.16	± 0.65	6.71	± 0.67
Dg	mm	7.63	± 0.88	7.93	± 0.63	7.14	± 0.67
S	mm^2	185.23	± 2.60	198.39	± 2.90	161.55	± 9.71
Φ	%	89.80	± 3.30	79.70	± 2.11	85.39	± 1.89
P	g	0.40	± 0.12	0.25	± 0.05	0.39	± 0.08
U	%	67.6	± 0.86	66.3	± 0.34	67.1	± 0.12

*Explanation of symbols: *L* = longitudinal diameter; *W* = intermediate diameter; *T* = transversal diameter; *Dg* = mean geometric diameter; *S* = fruit surface area; *Φ* = sphericity; *P* = weight; *U* = fruit moisture content.

Table III - Mean and standard deviation of dimensional parameters of berries of the CPT 5, CPT 4 and RUM 4 varieties harvested at Sella & Mosca

Parameter *	Unit of measurement	CPT 5		CPT 4		**RUM 4**	
		mean	std dev.	mean	std dev.	mean	std dev.
L	mm	10.37	± 1.15	8.97	± 0.86	11.05	± 1.42
W	mm	8.12	± 0.12	7.37	± 0.24	8.12	± 0.45
T	mm	8.48	± 0.68	7.70	± 0.75	8.69	± 0.97
Dg	mm	9.04	± 0.72	8.08	± 0.73	9.39	± 1.05
S	mm^2	258.14	± 3.49	206.82	± 3.88	279.99	± 2.61
Φ	%	86.00	± 2.51	79.51	± 2.59	83.11	± 2.50
P	g	0.45	± 0.12	0.41	± 0.09	0.44	± 0.14
U	%	69.6	± 0.21	68.9	± 0.31	69.1	± 0.12

*Explanation of symbols: *L* = longitudinal diameter; *W* = intermediate diameter; *T* = transversal diameter; *Dg* = mean geometric diameter; *S* = fruit surface area; *Φ* = sphericity; *P* = weight; *U* = fruit moisture content.
(a) Median ± standard deviation.*

Considering the mean weight of the berries, it is observed that the heaviest ones are present at the Sella & Mosca site compared to Pozzo d'Ussi and the humidity content varies from a minimum of 66.3% (Pozzo d'Ussi) to a maximum of 69.6% (Sella & Mosca). The berry surface area in the non-irrigated field (table IV), varies from 161.5 mm^2 for the RUM 4 variety to 206.8 mm^2 for CPT 5. The same parameter in the berries harvested at Sella & Mosca varies from: 198.4 mm2 for CPT 4 to 279.9 mm2 for RUM 4. The means reveal significant differences (P< 0.05%). The differences are caused by varietal features and agronomic practices supporting cultivation; the Pozzo d'Ussi field was not irrigated and consequently the shrubs are more rustic.

Table IV - Comparison of fruit surface area (mm^2) in the berries harvested at Pozzo d'Ussi

Cultivar	Number of samples	Means within groups	Homogeneous groups
RUM4	284	161.55	X
CPT4	284	185.23	X
CPT5	284	206.82	X
	Comparison of groups	Difference	Limits (+/-)
CPT5	CPT5 – CPT4	*21.58	11.17
RUM4	CPT5 – RUM4	*45.26	11.17
CPT4	CPT4 – RUM4	*23.68	11.17

* the differences between the groups are significant for *P*< 0.05%

5.2 Comparison between surface area (*S*) and weight (*P*) of the myrtle berries

The berries of the three varieties harvested at Pozzo d'Ussi had weight classes from 0.26g to 0.45g; among these, those with weights between 0.36g and 0.45g represented 80% of the sample considered. The S parameter for these fruits varied from a minimum of 130mm^2 to above 260 mm^2 (RUM 4). The surface area is constantly above the minimum value determined (130 mm^2). In the case of the irrigated fruits at Sella & Mosca, two differences appeared: the first concerns weight; the varieties CPT 5 and RUM 4 are in the same weight class as those at Pozzo d'Ussi (from 0.30g to 0.60g, for 70% of the berries harvested). The variety CPT 4 instead has fruits weighing between 0.20g and 0.40g (70% of the berries harvested). As concerns S, this varies from 180 mm^2 of CPT 4, to 340 mm^2 of CPT 5. Thus the use of irrigation produces, with the same weight, a noteworthy increase in fruit surface area owing to the different degree of humidity present in the berries (tables IV and Va and Vb).

5.3 Detachment force

The berries with an average weight above 0.20g harvested at Pozzo d'Ussi show detachment forces between 0.54 N (CPT 5) and 2.24 N (RUM 4). For the other weight classes, from 0.31g to 0.50 g, average detachment forces go from a minimum of 0.62 N to a maximum of 2.24 N in the CPT 5 variety. Berries with an average weight of 0.20g, harvested at Sella & Mosca, showed forces between 0.64 N and 0.80 N. For the other weight classes, from 0.31g to 0.50 g, variations from a minimum of 1.17 N for the variety RUM 4 to a maximum of 2.24 N for the same variety were observed.

5.4 Apparent Modulus of Elasticity (AME)

The feasibility of mechanical harvesting was evaluated by means of the apparent modulus of elasticity (Ea) (tables VI and VII). Analysis of the force/deformation diagram also shows that the berries have a resistance to compression identical to that of other fruits.

Table V - Weigth average (g), class percentage (%) and detachment force (N) measured in the first (a) and second (b) data of harvest in one experimental field

(a)

Varieties	Harvest data 3 december 2004 *"Pozzo d'Ussi"* Calculated parameters		
	Weight average (g)	Class weight (%)	Detachment Force (N)
CPT 4	0.27 ± 0.04	20[a]	1.27± 0.44
CPT5	0.26 ± 0.03	45	1.35± 0.25
RUM 4	0.29 ± 0.02	6	2.14± 0.54
CPT 4	0.36 ± 0.03	70	1.41± 0.38
CPT5	0.34 ± 0.03	45	1.33± 0.43
RUM 4	0.35 ± 0.03	83	2.24± 0.48
CPT 4	0.43 ± 0.03	10	1.12± 0.23
CPT5	0.42 ± 0.01	10	1.16± 0.09
RUM 4	0.42 ± 0.01	11	1.77± 0.68

(b)

Varieties	Harvest data 16 december 2004 *"Pozzo d'Ussi"* Calculated parameters		
	Weight average (g)	Class weight (%)	Detachment Force (N)
CPT 4	0.28 ± 0.01	20	0.90 ± 0.17
CPT 4	0.34 ± 0.03	70	1.04 ± 0.38
CPT 4	0.42 ± 0.03	10	1.20 ± 0.08
CPT 5	0.47 ± 0.03	60	0.54± 0.33
RUM 4	0.46 ± 0.03	45	1.95± 0.35
CPT 5	0.53 ± 0.03	35	0.62± 0.28
CPT 5	0.61 ± 0.11	5	0.30± 0.03

There appear two flexure points characteristic of the compression curve, one after about 120 seconds from application of pressure (deformation to yield) and the other after 140 seconds which identifies the value of N at rupture of the epicarp (deformation to rupture). Both are determined by the relation between the time of action of the force (s) and the velocity of advancement of the crossbar (mm/s). In both the experimental areas, RUM 4 compared to CPT 4 and CPT 5 shows that it is best suited for mechanical harvesting since its resistance to compression was in all cases higher, 59.41 kPa at Pozzo d'Ussi and 51.29 kPa at Sella & Mosca.

Table VI - Value of apparent elasticity (Ea = kPa/mm^2) observed on homogeneous planes for berries harvested at Pozzo d'Ussi

Cultivar	Number of samples	Means between groups	Homogeneo-us groups
CPT5	84	55.02 (kPa)	X
RUM4	84	59.41 (kPa)	X
CPT4	84	59.60 (kPa)	X
	Comparison between groups	Difference	Limits (+/-)
CPT5	CPT5 – RUM4	*-4.59	1.02
RUM4	RUM4 – CPT4	0.19	1.02
CPT4	CPT5 – CPT4	*-4.39	1.02

* the differences between the groups are significant for $P< 0.05\%$

Table VII - Value of apparent elasticity (E = kPa/mm^2) observed on homogeneous planes for berries harvested at Sella & Mosca

Cultivar	Number of samples	Means within groups	Homogeneo-us groups
CPT4	84	55.55 (kPa)	X
RUM4	84	59.29 (kPa)	X
CPT5	84	59.65 (kPa)	X
	Comparison between groups	Difference	Limits (+/-)
CPT4	CPT4 – RUM4	*-3.74	0.89
CPT5	CPT4 – CPT5	*-4.10	0.89
RUM4	CPT5 – RUM4	0.36	0.89

* the differences between the groups are significant for $P< 0.05\%$

They indicate better resistance of RUM 4 to external dynamic stresses caused by contact with the harvesting machine (shaking, impactscaused by vibrations and during the filling of bags and so on). There is also a greater predisposition of the berries to undergo minor abrasions, surface injuries and in general traumatic breaks in the fruit

surface which are the cause of enzymatic oxidation that reduces product quality. The varieties harvested at Sella & Mosca show the same significant differences and, of the three varieties, RUM 4 and CPT 4 have better resistance to dynamic compression that does CPT 5.

5.5 Biometric analysis of leaves and determination of terminal velocity (*Vt*)

By exploiting the different leaf areas, we can determine the operational parameters necessary for a ventilator installed to remove leaves that fall during plant vibration by the working organs (teeth of the comb).

Table VIII - Mean and standard deviation of dimensional parameters of leaves of the CPT 5, CPT 4 and RUM 4 myrtle varieties harvested at Sella & Mosca

Parame-ter*	Unit of measure-ment	RUM 4		CPT 4		CPT 5	
		mean	Std dev.	mean	Std dev.	mean	Std dev.
L	mm	25.13	± 5.04	22.59	± 5.78	30.51	± 6.48
W	mm	10.59	± 1.58	8.17	± 1.84	10.07	± 1.95
T	mm	11.95	± 2.49	9.96	± 2.16	11.64	± 2.19
Dg	mm	14.31	± 2.48	12.17	± 2.64	15.23	± 2.86
S	mm^2	642.99	± 1.09	47.06	± 1.23	73.33	± 1.21
Φ	%	57.85	± 0.40	49.20	± 2.11	49.91	± 1.51
P	g	0.06	± 0.02	0.05	± 0.02	0.08	± 0.03

*Explanation of symbols: *L* = longitudinal diameter; *W* = intermediate diameter; *T* = transversal diameter; *Dg* = mean geometric diameter; *S* = leaves surface area; *Φ* = sphericity; *P* = weight leaves.

Table IX - Mean and standard deviation of dimensional parameters of leaves of the CPT 5, CPT 4 and RUM 4 myrtle varieties harvested at Sella & Mosca

Cultivar	Number of samples	Terminal velocity (min)	Terminal velocity (max)
		(m/s)	(m/s)
CPT4	84	1.31	1.40
RUM4	84	0.54	0.61
CPT5	84	0.88	0.97

The mean values of parameters calculated also for the leaves at the Sella & Mosca site and their standard deviations are illustrated in (table VIII). For L, they are 25.13 mm, 22.59 mm and 30.51 respectively for the RUM 4, CPT 4 and CPT5 varieties. The values of W and T are 9.96 mm and 11.67 mm for the second. Leaf Dg was 14.5 4mm for RUM 4, 12.17 mm for CPT 4 and 15.23 mm for CPT 5. Leaf area varies from a minimum of 728.33 mm2 in RUM 4 to a minimum of 456.06 mm2 in CPT4. The shape of the leaves, defined by parameter (Φ), is different for all varieties and varies from 57.85% for RUM 4 to a minimum of 49.20% for CPT 4, while the heaviest leaves are those of the varieties CPT 5 and RUM 4. Terminal air velocity (Vt) varies with the variety and leaf surface; the minimum is between 0.54 m/s for RUM 4 and 1.31 m/s for CPT 4, while the maximum is between 0.61 m/s and 1.40 m/s (table IX).6

CONCLUSION

In designing facilitating machinery and mechanical systems for the harvesting of small fruits such as myrtle berries, the different physical dimensions of the fruits must be taken into account. These appear to be more delicate and less aggressive respect the traditional “finger” harvester and its protection by silicon sheaths may reduce berry damage. It is evident that the use of proper and consolidated farming practices (irrigation, fertilization and so on) improve the biometric characteristics of the fruits, lead to significant increases in mean geometric diameter (Dg), sphericity (Φ) and surface area (S) of the single fruits and consequently lead to more efficient use of harvesting systems. In the two experimental plots and for all varieties the difference in detachment force is minimum. The RUM 4 variety shows greater resistance to rupture and is thus better suited for mechanical harvesting by the electrical com with protected “fingers”. Increases in fruit size cause an increase in resistance to deformation and rupture of the epicarp. The berries are capable of resisting compression stresses from a minimum of 55 kPa (CPT 5) to a maximum of 59 kPa (RUM 4). All berries harvested are whole and without rupture of the epicarp, and only in a few cases was there crushing; this was found in the harvesting of all three varieties and in both experimental fields. The result of rupture test presented from others authors [11] show that the rupture forces is highly dependent on moisture content of the fruits. In the field irrigated and not irrigated the difference was very low, because the difference in moisture content from the berries was not significant. Myrtle plants are also characterized by a natural dropping off of leaves during the harvest period. In previous studies an increase in the percentage of leaves in the total harvest was observed. For separation of leaves from the fruit, the terminal air velocity (Vt) is dependent on leaf surface exposed to the air flow used and the variety: a velocity of 0.54 m/s (RUM 4) is sufficient to separate the leaves from the berries, while the maximum velocity is 1.40 m/s measured for the leaves of the CPT 4 variety. Finally, of the varieties tested, RUM 4, with and without irrigation, showed an excellent propensity for mechanical harvesting since it is the most resistant to impacts and handling of the product of the two different growing systems. Small harvester, which were designed for low or young bushes, appear also to reduce berry damage. Since damage is proportional to the distance berries fall, shorter bushes and smaller harvester may provided a higher quality fresh product.

REFERENCES

[1] Tutin G., *Flora Europaea*. Cambridge University Press, Cambridge, 1964.

[2] Valsecchi F., Camarda I., Piccoli arbusti, liane e suffrutici spontanei della Sardegna. Sassari, Carlo Delfino, 1990.

[3] Mulas M., Cani M.R., Pank F., Variability of rooting ability of softwood cuttings in myrtle germplasm. *Proceedings of the International Symposium on Breeding Research on Medicinal and Aromatic Plants*, Vol. 2, no. 1, pp. 191-194, 1996.

[4] Mulas M., Problematiche legate alla coltivazione del mirto. *Italus Hortus*, 11(4), pp. 308-312, 2004.

[5] Paschino F., Gambella F., Pinna G., La meccanizzazione della raccolta del mirto. *Atti della Terza Giornata di Studio sul Mirto*, Sassari, 23 Settembre 2005, pp. 43-50.

[6] Gambella F., Paschino F., Forze di distacco e di compressione delle bacche di mirto per la razionalizzazione di sistemi meccanici per la raccolta. *Atti Convegno Nazionale III, V e VI sezione A.I.I.A. "Tecnologie innovative nelle filiere: orticola, vitivinicola e olivicolo-olearia"*, Pisa-Volterra 5-7 Settembre 2007, Vol. IV, pp. 39-43.

[7] Dale A., Mechanical harvesting of berry crops. Chapter 1, pp. 270-271, 1988.

[8] McNicol R.J., Mechanical harvesting of berry crops. Chapter 1, pp. 283-291, 1988.

[9] Ozguven F., Vursavus K., Some physical, mechanical and aerodynamic properties of pine (Pinus pinea) nuts. *Journal of Food Engineering*, Vol.68, pp. 191-196, 2005.

[10] Sitkei G, Mechanics of agricultural materials. Akademi, Kiado, Budapest, 1986.

[11] Aydin C, Musa Özcan M., Determination of nutritional and physical properties of myrtle (Myrtus communis L.) fruits growing wild in Turkey. *Journal of Food Engineering*,Vol. 79, pp. 453-458, 2007.

[12] Mohsenin N. N., Physical properties of plant and animal materials. *Gordon and Breach Science Publishers*, New York, l970.

[13] Baryeh E. A., Physical properties bambara groundnuts. *Journal of Food Engineering*, Vol.47, pp. 321-326, 2001.

[14] ASAE Standard: ASAE S368.1, Compression Test of Food Material of Convex Shape. *American Society of Agricultural Engineers*, St. Joseph, MI, USA, 1997.

ISSN 1590-8844
International Journal of Mechanics and Control, Vol. 11, No. 02, 2010

EPICYCLIC GEAR TRAIN DYNAMICS INCLUDING MESH EFFICIENCY

E. Galvagno

Dipartimento di Meccanica

Politecnico di Torino

ABSTRACT

The paper presents an epicyclic gear train dynamic mathematical model including mesh efficiency, bearings/seals losses and inertial effects. The mathematical model treats separately the mesh between sun and planets gears and the mesh between planets and ring gears. Two different ordinary efficiency values for each gear pair can be specified for forward and reverse power transmission through it. The mesh efficiency is inserted into the dynamic model through a change in the direction of the mean reaction force between tooth surfaces. The extension of the equations valid for ordinary gearing to elementary gear train with epicyclic arrangement is made by using the kinematic inversion. A formula for selecting the correct efficiency value, to be used in the model, depending on the direction of power flows along the epicyclic gear train is presented. Finally, in order to check the validity of the dynamic model proposed, a steady-state working condition is analysed in detail and the mesh efficiency resulting from a numerical simulation of the model is compared with analytical formulas.

Keywords: Epicyclic Gear Train, Planetary Gear Set, Mesh Efficiency, Modeling.

1 INTRODUCTION

Epicyclic gear train (EGT) dynamic modeling has recently become relevant to improve the performance of virtual analysis especially in the field of automotive transmissions components [5]. The requirements which currently characterize the transmission design from the point of view of vehicle energy saving ask for gear trains dynamic virtual analysis including a detailed description of the power losses.

As well kwon the main sources of power loss in a gear train are: gear mesh losses, windage and churning losses, bearing and seal losses and lubrication pump losses.

In comparison with ordinary gear trains where mesh efficiency is very often close to unity, the power loss in an epicyclic gear train, depending both on the operating condition and on the gear train geometrical configuration, can become very low [6].

Contact author: Enrico Galvagno

C.so Duca degli Abruzzi, 24
10129 Torino, Italy
enrico.galvagno@polito.it

Several articles were written with the aim of analytically describe the efficiency of such a mechanical device for all the possible power paths through the gearing. Pennestrì and Valentini in [7] summarize some of these analytical approaches, e.g. [4], [8] and [9], for the mesh efficiency computation in a two degrees of freedom (d.o.f.) epicyclic gear train and demonstrate the numerical equivalence of the different formulas presented. The problem of the extension of these analytical expressions for a generic n-link EGT can be dealt with by means of manual (see e.g. [10]) and systematic methods (see e.g. [6]).

A systematic methodology for computing the mechanical efficiency of a generic EGT considering also load dependant power losses and inertia effect is presented in [2]. In that work the multibody formalism is used for solving the inverse dynamic problem in gear train and the approximated method of Anderson and Lowenthal [11], that accounts for sliding, rolling, bearing and windage losses, is adopted for estimating the efficiency of the ordinary gear train.

The present work shows a dynamic model of a two d.o.f. epicyclic gear train that considers the following source of internal power loss: mesh efficiency, seals and bearings. The inertial effects of all the components are also included in the model.

The followed approach consists in the next steps:

- decomposition of the gear train in its basic elements
- insertion of the mesh efficiency for each gear pair through a change in the direction of the mean reaction force between tooth surfaces [4]
- estimation of the ordinary efficiency of the gear pairs as function of gears geometrical parameters and the frictional contact conditions between teeth, see e.g. [1], [3], [4], [11], [12]. This part is not detailed in the paper.
- extension of the formulae valid for ordinary gear train to elementary gear train with epicyclic arrangement [2]
- Coulomb friction model for the resistant torque due to bearings and seals
- dynamic balance equations starting from the free body diagrams and kinematic relations
- dynamic system matrix formulation and solution
- efficiency expression valid for all possible power flow configurations
- graphical and numerical model verification in steady-state conditions

The paper discusses the relations between efficiency and displacement of the meshing force of the gears due to the presence of friction both for external and internal gears and an original formula is proposed to appropriately select the right instantaneous value depending on the specific dynamic situation.
The model presented was implemented in a simulation environment and the correctness of the computed mesh efficiency was verified for all the possible combinations of power flows. The simulated efficiency using the proposed dynamic model and the analytical formulas [7] give exactly the same results for the same steady state operating conditions. A particular case is analysed in detail considering the awaited (graphically) and the computed model variables (analytically) with the aim of verifying the sign of the internal meshing forces and their displacement from the pitch point.

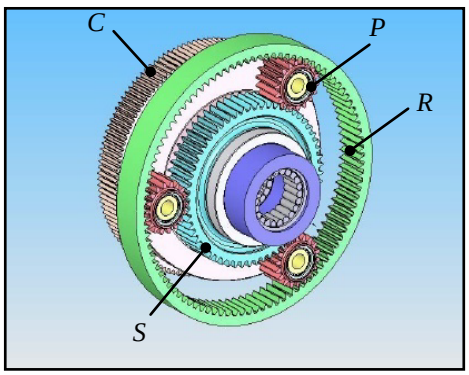

Figure 1- Epicyclic gear train with the adopted nomenclature

2 MESH EFFICIENCY MODELING FOR ORDINARY GEARING

According to the Merritt's model [4], the direction of the meshing force, in presence of friction between teeth, intersects the center distance in a point, which is not the center of instantaneous rotation of the involved pitch circles. Since this distance is not constant, during the passage of the point of contact from end to end of the line of contact, it is useful to compute a mean value of this displacement over a complete cycle of engagement called δ.
Generally speaking, in case of different meshing conditions, i.e. sliding velocities and coefficient of frictions, in approach and recess there can be differences in terms of direct (subscript *D*) and inverse (subscript *I*) mesh efficiency. Considering for example the same gears used both as a reduction drive and as a step-up drive, thus replacing the driver with the follower, different values of efficiency can arise. More specifically, as explained in [3], when the recess action of the driver on a reduction drive is greater than the approach action, then the corresponding step-up drive will be less efficient than the reduction drive. Thus, it is important to allow the definition of different efficiency values η_{Dij} and η_{Iij} respectively for forward and reverse power transmission through the gears, that can be generally different. The last two subscripts used both for efficiency and displacement specify the driving gear (*i*) and the driven gear (*j*) in the direct configuration.
Figure 1 shows a common planetary gear set assembly with sun (*S*), planets (*P*), planet carrier (*C*) and ring (*R*). The Figure presents a typical example of gears configuration where there are meshing between both external gears (sun-planet) and internal gears (planet-ring).
The relations between the efficiency and the displacement of the meshing force due to the presence of friction, both for external and internal gears, are now discussed. Considering the mesh that involves the sun and planet gears (external gears), the relation between displacement and efficiency can be formulated as:

$$\delta_{Dsp} = \frac{1 - \eta_{Dsp}}{\frac{\eta_{Dsp}}{R_s} + \frac{1}{R_p}} \qquad \delta_{Isp} = \frac{1 - \eta_{Isp}}{\frac{\eta_{Isp}}{R_p} + \frac{1}{R_s}} \tag{1}$$

where the variables referred to the sun and to the planets are indicated respectively by subscripts *s* and *p*. R_s , R_p and R_r are the pitch circle radius of sun, planets and ring, while R_c is the distance between the center of EGT and the center of planets in the considered epicyclic arrangement. The direct efficiency η_{Dsp} corresponds to the case of planet driven by sun.
The offset displacement of the ordinary gear train composed by the planet (external gear) and the ring (internal gear) can be calculated as:

$$\delta_{Dpr} = \frac{\left(1 - \eta_{Dpr}\right)}{\frac{\eta_{Dpr}}{R_p} - \frac{1}{R_r}} \qquad \delta_{Ipr} = \frac{\left(1 - \eta_{Ipr}\right)}{\frac{1}{R_p} - \frac{\eta_{Ipr}}{R_r}} \tag{2}$$

where subscript *r* refers to the ring. The direct efficiency η_{Dpr} corresponds to the case of planet as driving gear and ring as the driven one. Once calculated and stored the direct (δ_{Dij}) and inverse (δ_{Iij}) displacement values for each gear pair, it is necessary to appropriately select the right instantaneous value depending on the specific dynamic situation.

3 MESH EFFICIENCY MODELING FOR EPICYCLIC GEAR TRAIN

Equations (1) and (2) are obtained considering the mesh between two gears with their axes fixed in the space, i.e. ordinary gear train, but the same equations can be applied also to a planetary gear set, where there is a carrier that moves the axes of the planet gears. It must be considered in that case, instead of the real absolute velocity, the velocity of the gears relative to the carrier speed; a kinematic inversion in fact cannot affect the power losses [2].
More specifically, if the tangential component of the meshing force exerted by gear *j* on gear *i*, indicated in the equations and Figures with F_{tji}, has the same direction as the relative pitch tangential speed (or the same sign of the angular speed of gear *i* relative to the carrier arm *c*, i.e. $\omega_{i,rel}$), the *i* component is the follower of the basic train under a kinematic inversion which makes the gear carrier fixed [7]. Conversely, if they have opposite directions, gear *i* is the driver.
The expressions proposed in [5] were so extended including some new considerations explained in the following. The non linear expressions of the offset distance, based on the convention of sign of Figure 3, can be computed as follows:

Sun-planet coupling:

$$\delta_{sp} = \mathrm{sgn}\left|F_{tps}\left(\omega_{p,rel} - \omega_{s,rel}\right)\right| \left(\delta_{Dsp}\, f_{-}(F_{tps}\, \omega_{s,rel}) + -\delta_{Isp}\, f_{+}(F_{tps}\, \omega_{s,rel})\right) \quad (3)$$

Planet-ring coupling:

$$\delta_{pr} = \mathrm{sgn}\left|F_{trp}\left(\omega_{r,rel} - \omega_{p,rel}\right)\right| \left(\delta_{Dpr}\, f_{-}(F_{trp}\, \omega_{p,rel}) + -\delta_{Ipr}\, f_{+}(F_{trp}\, \omega_{p,rel})\right) \quad (4)$$

where

$$f_{\pm}\left(F_{tji}\, \omega_{i,rel}\right) = \frac{1 \pm \mathrm{sgn}\left(F_{tji}\, \omega_{i,rel}\right)}{2} \quad (5)$$

and the relative speeds are

$$\begin{cases} \omega_{s,rel} = \omega_s - \omega_c \\ \omega_{r,rel} = \omega_r - \omega_c \\ \omega_{p,rel} = \omega_p - \omega_c \end{cases}$$

The former expressions of the offset distance can be extended to a generic case, considering gears *i* and *j*, where *i* is an external gear and *j* can be either an external or an internal gear.

The generic formula is:

$$\delta_{ij} = \mathrm{sgn}\left|F_{tji}\left(\omega_{j,rel} - \omega_{i,rel}\right)\right| \left(\delta_{Dij}\, f_{-}(F_{tji}\, \omega_{i,rel}) + -\delta_{Iij}\, f_{+}(F_{tji}\, \omega_{i,rel})\right) \quad (6)$$

where

$$\begin{aligned} \omega_{i,rel} &= \omega_i - \omega_k \\ \omega_{j,rel} &= \omega_j - \omega_k \end{aligned} \quad (7)$$

Figure 2 illustrates the two possible cases of meshing between external and internal gears. The carrier is represented as *k*.

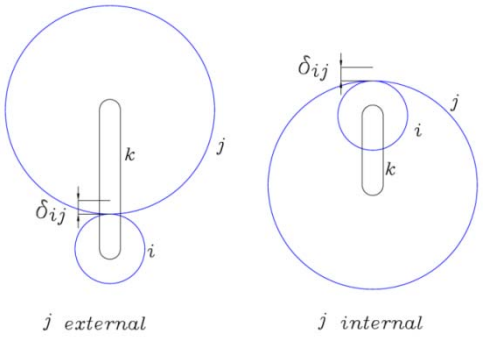

Figure 2- Offset distance positive sign convention for external (left) and internal gears (right).

The first part of expression (6), i.e. $\mathrm{sgn}\left|F_{tji}.\left(\omega_{j,rel} - \omega_{i,rel}\right)\right|$, is used to have null offset distance and consequently a unitary efficiency in two particular cases: when there are no forces exchanged between the gears ($F_{tji} = 0$), e.g. when the gears are completely unloaded, and when all the angular velocities of the gears are the same ($\omega_{j,rel} - \omega_{i,rel} = 0$). For instance, when $\omega_s = \omega_r = \omega_p = \omega_c$, the epicyclic gear train behaves like a unique component and the absence of relative motions involves that the loss in the teeth contacts is null.
The second part of equation (6) accounts for all the other working conditions of the epicyclic gear pair. A specific function, $f_{\pm}$, is introduced in order to alternatively activate or deactivate one of the two addends (the direct and inverse displacements) depending on the sign of the power of the ordinary gearing obtained through a kinematic inversion which makes the planet carrier fixed.
An example of a possible operating condition covered by equations (3) and (4) appears when ω_s is null, i.e. the sun is blocked ($\omega_{p,rel} \neq \omega_{s,rel}$). Since the sun cannot deliver power at null speed, for sun-planet coupling the only possible driving gear is the planet and so eq. (3) should give the inverse displacement. Indeed, the meshing force of contact that acts on the sun gear causes a moment concordant with the sun relative angular velocity ($f_{+} = 1$, $f_{-} = 0$), then, the offset displacement is negative, i.e. inside of the sun pitch circle: $\delta_{sp} = -\delta_{Isp}$.

4 BEARINGS AND SEALS MODEL

The analytical formulations of mechanical efficiency of ordinary and epicyclic gear trains usually consider only meshing losses. In the proposed dynamics equations further dissipative terms, such as bearings and seals resistant torques, are taken into account for all the four components (sun, planet, carrier and ring). These contributions, called T_B, are defined opposite with respect to the angular velocity difference between the inner and the outer ring of the considered bearing. Thus it is important to correctly define the position of bearings and seals among the epicyclic assembly. A Coulomb friction model is adopted for the torque computation in order to take into account the possible change in the direction of rotation of the specific component. Considering in this case that the bearings of the ring are mounted between the ring gear shaft and the sun gear shaft, then the relative angular velocity between them is introduced as the argument of a sign function in the equations. The sun gear and the carrier are supported through bearings connected to the gearbox housing. Consequently the bearings and seals torques are:

$$\begin{cases} T_{Brs} &= |T_{Brs}|\ \mathrm{sgn}(\omega_r - \omega_s) \\ T_{Bs} &= |T_{Bs}|\ \mathrm{sgn}(\omega_s) \\ T_{Bc} &= |T_{Bc}|\ \mathrm{sgn}(\omega_c) \\ T_{Bpc} &= |\ T_{Bpc}|\ \mathrm{sgn}(\omega_p - \omega_c) \end{cases}$$

where for instance T_{Brs} stands for the bearings and seals torque acting on the ring shaft. The third subscript is introduced only if the bearing is placed between two moving elements of the gearing, otherwise, if is fixed to the ground, it is omitted.

5 EGT KINEMATICS AND DYNAMICS

5.1 SIGN CONVENTIONS

As can be seen in Figure 3, the absolute angular velocities (and accelerations) of sun, ring, planet and carrier are assumed positive if they rotate in clockwise direction and the same applies to the torques.

The tangential component of the meshing force is positive if causes a clockwise moment with respect to the center of the planetary gear set (point *O* in Figure 3).

The offset distance δ_{sp} for sun-planet coupling, being both external gears, is assumed positive if located on the outside of the sun gear pitch circle and its instantaneous value is computed using equation (3). For planet-ring coupling, internal gears, the offset distance δ_{pr} (see eq. (4)) is assumed positive if located on the outside of the planet gear pitch circle, thus representing the case when it is the driving gear.

5.2 KINEMATIC EQUATIONS

The kinematic relation between the epicyclic gear train speeds can be expressed through the following matricial equation:

$$\begin{Bmatrix} \omega_c \\ \omega_p \end{Bmatrix} = \begin{bmatrix} \frac{R_r}{2R_c} & \frac{R_s}{2R_c} \\ \frac{R_r}{2R_p} & -\frac{R_s}{2R_p} \end{bmatrix} \begin{Bmatrix} \omega_r \\ \omega_s \end{Bmatrix} = [K] \begin{Bmatrix} \omega_r \\ \omega_s \end{Bmatrix} \tag{8}$$

5.3 DYNAMIC EQUATIONS

Considering the free body diagrams of ring, sun, carrier and planets represented in Figure 3 the dynamic equations written in matrix form are:

$$[I]\{\dot{\omega}\} = \{T\} - \{T_B\} + n_p[G]\{F_t\} \tag{9}$$

where $[I]$ is the inertia matrix, $\{\dot{\omega}\}$ is the acceleration vector, $\{T\}$ and $\{T_B\}$ are respectively the vector of input torques and the one of bearings and seals torques, n_p is the number of planets, $[G]$ is a geometric matrix containing the radii of all the epicyclic elements and the displacements of the meshing forces, $\{F_t\}$ is the vector of the tangential components of the meshing forces.

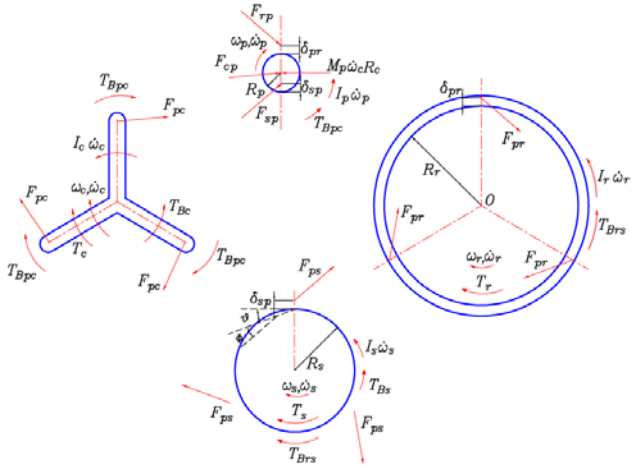

Figure 3- Free body diagrams of the planetary gear train

The additional equation to compute the tangential force exerted by the carrier on each planet is:

$$F_{tcp} = -F_{trp} + F_{tps} + M_pR_c\dot{\omega}_c \tag{10}$$

Equation (9) can be expanded in the following form:

$$\begin{bmatrix} I_r & & & \\ & I_s & & \\ & & (I_c + n_p\,M_p\,R_c^2) & \\ & & & n_pI_p \end{bmatrix} \begin{Bmatrix} \dot{\omega}_r \\ \dot{\omega}_s \\ \dot{\omega}_c \\ \dot{\omega}_p \end{Bmatrix} = \begin{Bmatrix} T_r \\ T_s \\ T_c \\ 0 \end{Bmatrix} + \\ - \begin{Bmatrix} |T_{Brs}|\ \mathrm{sgn}(\omega_r - \omega_s) \\ |T_{Bs}|\ \mathrm{sgn}(\omega_s) - |T_{Brs}|\ \mathrm{sgn}(\omega_r - \omega_s) \\ |T_{Bc}|\ \mathrm{sgn}(\omega_c) - n_p|\ T_{Bpc}|\ \mathrm{sgn}(\omega_p - \omega_c) \\ n_p|T_{Bpc}|\ \mathrm{sgn}(\omega_p - \omega_c) \end{Bmatrix} + \\ +n_p \begin{bmatrix} -(R_r + \delta_{pr}) & 0 \\ 0 & R_s + \delta_{sp} \\ R_c & -R_c \\ R_p + \delta_{pr} & R_p - \delta_{sp} \end{bmatrix} \begin{Bmatrix} F_{trp} \\ F_{tps} \end{Bmatrix} \tag{11}$$

5.4 SOLUTION OF THE MOTION EQUATIONS

In order to integrate the system of non-linear differential equations (11), ring and sun angular accelerations are chosen as independent variables.

Therefore, eq. (11) can be separated into two parts:

$$[I_{rs}]\begin{Bmatrix}\dot{\omega}_r\\ \dot{\omega}_s\end{Bmatrix} = \{T_{rs}\} - \{T_{Brs}\} + n_p[G_{rs}]\begin{Bmatrix}F_{trp}\\ F_{tps}\end{Bmatrix} \quad (12)$$

$$[I_{cp}]\begin{Bmatrix}\dot{\omega}_c\\ \dot{\omega}_p\end{Bmatrix} = \{T_{cp}\} - \{T_{Bcp}\} + n_p[G_{cp}]\begin{Bmatrix}F_{trp}\\ F_{tps}\end{Bmatrix} \quad (13)$$

An expression for meshing forces vector can be found starting from equations (8), (12) and (13). By substituting the derivative of eq. (8) into (13) and pre-multiplying the resulting equation by $[K^{-1}I_{cp}^{-1}]$ it yields:

$$\begin{Bmatrix}\dot{\omega}_r\\ \dot{\omega}_s\end{Bmatrix} = \left[K^{-1}\, I_{cp}^{-1}\right]\left(\{T_{cp}\} - \{T_{Bcp}\} + n_p[G_{cp}]\begin{Bmatrix}F_{trp}\\ F_{tps}\end{Bmatrix}\right)$$

Then, the previous equation can be pre-multiplied by I_{rs} and substituted into eq. (12):

$$[I_{rs}K^{-1}I_{cp}^{-1}]\left(\{T_{cp}\} - \{T_{Bcp}\} + n_p[G_{cp}]\begin{Bmatrix}F_{trp}\\ F_{tps}\end{Bmatrix}\right) = \{T_{rs}\} + -\{T_{Brs}\} + n_p[G_{rs}]\begin{Bmatrix}F_{trp}\\ F_{tps}\end{Bmatrix}$$

Making some algebraic steps with the aim of isolating the vector of meshing forces it results:

$$n_p[I_{rs}K^{-1}I_{cp}^{-1}G_{cp} - G_{rs}]\begin{Bmatrix}F_{trp}\\ F_{tps}\end{Bmatrix} = \left\{T_{rs} - T_{Brs} + -[I_{rs}K^{-1}I_{cp}^{-1}]\{T_{cp} - T_{Bcp}\}\right\}$$

Then, pre-multiplying by $\left[I_{rs}K^{-1}I_{cp}^{-1}G_{cp} - G_{rs}\right]^{-1}$ and dividing by n_p , the vector of meshing forces can be computed as:

$$\begin{Bmatrix}F_{trp}\\ F_{tps}\end{Bmatrix} = \frac{1}{n_p}\left[I_{rs}K^{-1}I_{cp}^{-1}G_{cp} - G_{rs}\right]^{-1}\left\{T_{rs} - T_{Brs} + -[I_{rs}K^{-1}I_{cp}^{-1}]\{T_{cp} - T_{Bcp}\}\right\} \quad (14)$$

Finally, to evaluate the ring and sun gears dynamics, the following equation has to be integrated:

$$\begin{Bmatrix}\dot{\omega}_r\\ \dot{\omega}_s\end{Bmatrix} = [I_{rs}]^{-1}\left(\{T_{rs}\} - \{T_{Brs}\} + n_p[G_{rs}]\begin{Bmatrix}F_{trp}\\ F_{tps}\end{Bmatrix}\right) \quad (15)$$

Dynamic equations (14) and (15) together with kinematic equation (8) are the final equations that can be implemented in a simulation environment for the virtual analysis of the dynamic system. They completely describe the kinematic and dynamic behavior of the epicyclic gear train with mesh efficiency and bearings/seals losses.

It must be noted that the presence of friction between the tooth surfaces generates an algebraic loop in the model. In fact, eq. (6) is an algebraic relation between tangential force and displacement. Since the values of displacements (δ_{sp} and δ_{pr}) must be known in order to compute the geometric matrices (G_{rs} and G_{cp}), and furthermore since these matrices appear also in the final expression of the tangential forces (14), it is evident that the problem exists. Thus, the system of equations can be iteratively solved, starting from the retained force values from the last iteration at the previous time step.

6 STEADY-STATE MODEL VERIFICATIONS

In order to check the validity of the dynamic model proposed in steady-state conditions, in this section an example of epicyclic gear set operation will be analysed in detail. More specifically both the dynamic equations (11) and the offset distance equations (3) and (4) are verified. During the considered tests, all the angular accelerations are set to zero, i.e. the four components are in equilibrium with constant external torques at constant speeds.

Moreover mesh efficiency numeric values, obtained in steady-state conditions, were compared with the results of analytical formulations [7].

6.1 GRAPHICAL MODEL VERIFICATION

The distribution of power between the epicyclic gear train elements for the analysed configuration is resumed in Table I.

Table I – Working condition analysed

Case	Input Gear	Output Gear	Fixed Gear
A	S , R	C	-

The power enters into the system both through the sun and through the ring gear, while it goes out from the carrier. To completely define the working condition of the EGT with the aim of describing its efficiency it is necessary to specify not only the power flow direction through the EGT but also the specific kinematic situation analysed [7]. Here it is assumed that the angular velocities of the sun and the ring have the same positive direction of rotation and that $\omega_r > \omega_s$. The kinematics of this mechanism is illustrated in Figure 4, together with the kinematic inversion that makes fixed the planet carrier; the velocities of the gears relative to the carrier are shown by black triangles.

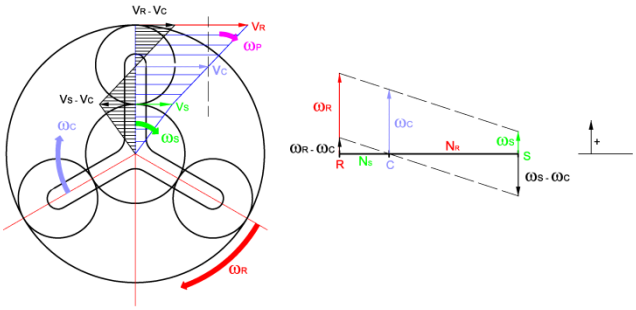

Figure 4 - Kinematics of Case A: Speeds distribution (to the left) and lever analogy (to the right).

The equilibrium of the EGT members is depicted in Figure 5. It is of interest to note that, despite the sun is a driver for the EGT, i.e. $T_s\omega_s > 0$, its relative angular velocity is

negative, therefore the product $T_s(\omega_s - \omega_c) < 0$. This negative power value identifies the driven gear under the kinematic inversion which makes the gear carrier fixed.

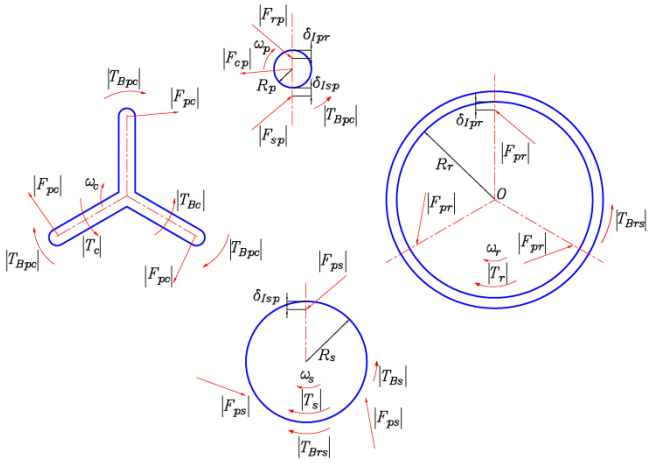

Figure 5 - Equilibrium of the EGT elements considering Case A. The modulus is introduced in order to pick out the real direction of forces, speeds and torques.

It is possible to verify the validity of (3), (4) and (11), by substituting the correct signs of forces, torques and angular velocities and comparing them with the awaited results reported in Figure 5.

It was assumed that ω_s and ω_r have positive sense of rotation (clockwise), than by kinematics relation (8), it results that ω_p and ω_c have positive sense too and $\omega_p > \omega_c$.

The tangential force exerted by the planet on the ring can be obtained starting from the dynamic equation of ring, i.e. first row of matrix equation (11), neglecting the inertial contribution and putting in evidence the absolute values of the single terms:

$$F_{tpr} = -F_{trp} = \frac{-|T_r| + |T_{Brs}|}{n_p\,(R_r + \delta_{pr})} \tag{16}$$

It must be observed that the absolute values are introduced, both in equations and in figures, with the aim of facilitating the sign discussion of the results. Since the ring is a driver, the torque T_r has the same direction of its angular velocity and therefore its value is also positive, i.e. $T_r = |T_r|$. Neglecting the dissipative terms, different from the mesh loss, i.e. $T_{Brs} = 0$, consequently F_{tpr} is negative. The graphical equilibrium reported in Figure 5 confirms the analytical solution obtained using the model.

The sun is a driver too, therefore once again torque T_s has to have the same direction of its angular velocity and therefore its value is positive. Starting from the dynamic equation of the sun, i.e. second row of matrix equation (11), the tangential force exerted by each planet on the sun is:

$$F_{tps} = \frac{-|T_s| + |T_{Bs}| - |T_{Brs}|}{n_p\,(R_s + \delta_{sp})} \tag{17}$$

Neglecting the effect of bearing torques, this force is negative too, in agreement with Figure 5.

The meshing forces acting on the planet are the opposite of those calculated before using eq. (16) and (17), that is they both are positive. Thus, they are coherent with the representation in Figure 5.

The third row of matrix equation (11) together with eq.(10) considering also that T_c is negative since it is the follower, i.e. $T_c = -|T_c|$, allows to calculate the tangential component of force that carrier applies to each planet:

$$F_{tcp} = \frac{-|T_c| - |T_{Bc}| + n_p|T_{Bpc}|}{n_p R_c} \tag{18}$$

In accordance with Figure 5 it shows a negative value.

As mentioned before, in order to calculate the offset distances, it's necessary to make the epicyclic gear train into ordinary gear train through a kinematic inversion, i.e. the angular speeds relative to the carrier must be considered. Referring to Figure 4, the relative velocity of the sun is negative, i.e. $(\omega_s - \omega_c) < 0$, and the meshing force exerted by the planet on the sun F_{tps} is negative too. Eq. (5) with i=s and j=p gives:

$$f_{\pm}(F_{tps}\;\omega_{s,rel}) = \frac{1 \pm \mathrm{sgn}(F_{tps}\;\omega_{s,rel})}{2} = \begin{cases} \frac{1+1}{2} = 1 \\ \frac{1-1}{2} = 0 \end{cases} \tag{19}$$

Being also

$$F_{tps} \neq 0 \;\;\&\;\; \omega_{p,rel} \neq \omega_{s,rel}$$

it follows that

$$\mathrm{sgn}\left|F_{tps}(\omega_{p,rel} - \omega_{s,rel})\right| = 1 \tag{20}$$

Thus, substituting these values (19) and (20) into eq. (3) one obtains $\delta_{sp} = -\delta_{Isp}$.

Repeating the same analysis to the contact between planet and ring, it's possible to observe that the relative velocity of planet is positive and the meshing force F_{trp} is positive too. Thus, substituting the values into eq. (4), the offset displacement will be equal to $\delta_{pr} = -\delta_{Ipr}$, as it is represented in Figure 5.

6.2 MESH EFFICIENCY NUMERICAL VALIDATION USING ANALYTICAL METHODS

The EGT dynamic model was implemented in a commercial modeling and simulation environment and the mesh efficiency values, obtained in steady-state conditions, were compared with the results of analytical formulations [7]. Obviously for this purpose the bearing/seals resistant torques were set to zero.

The EGT dynamic model explained in the paper was coupled with one speed controller for each driving gear and one load for each driven gear of the EGT.

Feed-forward terms are calculated and applied to the EGT elements, both to driving and to driven gears. They consist in the torques required to satisfy the equilibrium of the EGT in case of steady-state conditions and unitary efficiency, i.e.

$$\begin{cases} T_{c,ff} = \left(1 + \frac{R_r}{R_s}\right) T_{s,ff} \\ T_{r,ff} = \frac{R_r}{R_s}\, T_{s,ff} \end{cases}$$

In order to compensate for the differences in the equilibrium torques, with respect to the ideal case, due to the internal losses of the gear train, a speed controller for each driving gear and a quadratic load for driven gears are added.
The load torque increases with the square of the difference between the instantaneous speed of rotation and the initial speed:

$$T_{i,load} = T_{i,ff} - k_i\,(\omega_i - \omega_{i0})^2\,\mathrm{sgn}(\omega_i - \omega_{i0})$$

where k_i is a proportionality constant.

Speed controller is composed by the sum of the feed-forward term and a PID feedback controller with the aim of keeping the controlled speed (ω_i) equal to its initial value (ω_{i0}):

$$T_{i,control} = T_{i,ff} + k_p\,(\omega_{i0} - \omega_i) + k_i \int (\omega_{i0} - \omega_i)dt + \\ + k_d \frac{d(\omega_{i0} - \omega_i)}{dt}$$

In this way, by specifying the initial conditions according to a specific power configuration to be analysed, thanks to load and speed controller, it is possible to reach the steady-state equilibrium of the system and compare the results of analytical methods with simulation. The efficiency of the EGT, defined as the ratio of the power that comes out of the system by the power that comes in, is computed through the following generic expression:

$$\eta = \frac{|P_{out}|}{|P_{in}|} = \\ = \frac{|T_r\,\omega_r|\,f_-(T_r\,\omega_r) + |T_s\,\omega_s|\,f_-(T_s\,\omega_s) + |T_c\,\omega_c|\,f_-(T_c\,\omega_c)}{|T_r\,\omega_r|\,f_+(T_r\,\omega_r) + |T_s\,\omega_s|\,f_+(T_s\,\omega_s) + |T_c\,\omega_c|\,f_+(T_c\,\omega_c)}$$

Once again the usage of function $f_\pm$ allows to define a unique efficiency equation for all the possible EGT working conditions. If the sign of the i-th power is positive, it means that represents power entering into the system and so must be placed at the denominator of the efficiency equation, otherwise if the product between speed and torque is negative it is an output power and so should be at the numerator.
All the possible working conditions in terms of power flows direction along the EGT were tested and the obtained simulation results are exactly the same of those obtainable using one of the method cited in [7].

7 CONCLUSIONS

An epicyclic gear train dynamic model including mesh efficiency, bearings/seals losses and inertial effects were presented in the paper. The validity of the proposed model for a specific steady state working condition was demonstrated by analyzing the internal forces of the mechanism. In addiction the mesh efficiency value of the epicyclic gear train resulting from numerical simulations of the model were compared with analytical formulas; all the possible working conditions in terms of power flows direction along the EGT were tested and the obtained results using the two methods are exactly the same. The same approach used to insert the dissipative terms into the analysed gearing layout can be extended for the study of more complex epicyclic and ordinary gear train configurations.

REFERENCES

[1] Yada T., Review of gear efficiency equation and force treatment. *JSME International Journal. Series C – Mechanical Systems Machine Elements and Manufacturing*, Vol.40, p. 1-8, 1997.

[2] Mantriota G. and Pennestrì E., Theoretical and experimental efficiency analysis of multi-degrees-of-freedom epicyclic gear trains. *Multibody System Dynamics*, Vol. 9, pp. 389-408, 2003.

[3] Buckingham E., *Analytical Mechanics of Gears*, McGraw Hill, p.395-406, 1949.

[4] Merritt H.E., *Gears.* 3rd edition, Sir Isaac Pitman & Sons, 1954.

[5] Velardocchia M., Bonisoli E., Galvagno E., Vigliani A., Sorniotti A., Efficiency of Epicyclic Gears in Automated Manual Transmission Systems. *Proc. of SAE ICE2007 8th Int. Conf. Engines for Automobile*, Capri 16-20, September 2007.

[6] Del Castillo J. M., The analytical expression of the efficiency of planetary gear trains. *Mechanism and Machine Theory*, Vol.37, pp. 197-214, 2002.

[7] Pennestrì E. and Valentini P.P., A review of formulas for the mechanical efficiency analysis of two degrees-of-freedom epicyclic gear trains. *ASME Journal of Mechanical Design*, p. 602-608, 2003.

[8] Radzimovsky E. I., How to find efficiency, Speed and Power in Planetary Gear Drives. *Machine Design*, pp.144-153, 1959.

[9] Maggiore A., The efficiency of epicyclic two d.o.f. gear train (in italian). *Proc. of I Congresso Nazionale di Meccanica Teorica ed Applicata*, Udine, Vol.3, pp.65-85, 1971.

[10] Müller H.W., Epicyclic Drive Trains: Analysis, Syntesis and Applications. *Wayne State University Press*, 1982.

[11] Anderson N. E. and Loewenthal S. H., Design of spur gear for improved efficiency. *ASME Journal of Mechanical Design*, Vol.104, pp.767-774, 1982.

[12] Niemann, G. and Winter, H., *Elementi di Macchine*, Vol. II, Springer, 1983.

ISSN 1590-8844
International Journal of Mechanics and Control, Vol. 11, No. 02, 2010

TEMPLATE FOR PREPARING PAPERS FOR PUBLISHING IN INTERNATIONAL JOURNAL OF MECHANICS AND CONTROL

Author1* Author2**

* affiliation Author1

** affiliation Author2

ABSTRACT

This is a brief guide to prepare papers in a better style for publishing in International Journal of Mechanics and Control (JoMaC). It gives details of the preferred style in a template format to ease paper presentation. The abstract must be able to indicate the principal authors' contribution to the argument containing the chosen method and the obtained results. (max 200 words)

Keywords: keywords list (max 5 words)

1 TITLE OF SECTION (E.G. INTRODUCTION)

This sample article is to show you how to prepare papers in a standard style for publishing in International Journal of Mechanics and Control.
It offers you a template for paper layout, and describes points you should notice before you submit your papers.

2 PREPARATION OF PAPERS

2.1 SUBMISSION OF PAPERS

The papers should be submitted in the form of an electronic document, either in Microsoft Word format (Word'97 version or earlier).
In addition to the electronic version a hardcopy of the complete paper including diagrams with annotations must be supplied. The final format of the papers will be A4 page size with a two column layout. The text will be Times New Roman font size 10.

Contact author: author1[1], author2[2]

[1]Address of author1.

[2]Address of author2 if different from author1's address.

2.2 DETAILS OF PAPER LAYOUT

2.2.1 Style of Writing

The language is English and with UK/European spelling. The papers should be written in the third person. Related work conducted elsewhere may be criticised but not the individuals conducting the work. The paper should be comprehensible both to specialists in the appropriate field and to those with a general understanding of the subject.
Company names or advertising, direct or indirect, is not permitted and product names will only be included at the discretion of the editor. Abbreviations should be spelt out in full the first time they appear and their abbreviated form included in brackets immediately after. Words used in a special context should appear in inverted single quotation mark the first time they appear. Papers are accepted also on the basis that they may be edited for style and language.

2.2.2 Paper length

Paper length is free, but should normally not exceed 10000 words and twenty illustrations.

2.2.3 Diagrams and figures

Figures and Tables will either be entered in one column or two columns and should be 80 mm or 160 mm wide respectively. A minimum line width of 1 point is required at actual size. Captions and annotations should be in 10 point with the first letter only capitalised *at actual size* (see Figure 1 and Table VII).

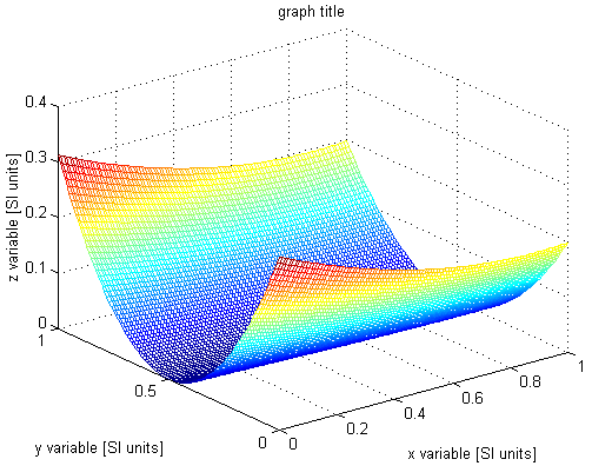

Figure 1 Simple chart.

Table VII - Experimental values

Robot Arm Velocity (rad/s)	Motor Torque (Nm)
0.123	10.123
1.456	20.234
2.789	30.345
3.012	40.456

2.2.4 Photographs and illustrations

Authors could wish to publish in full colour photographs and illustrations. Photographs and illustrations should be included in the electronic document and a copy of their original sent. Illustrations in full colour …

2.2.5 Equations

Each equation should occur on a new line with uniform spacing from adjacent text as indicated in this template. The equations, where they are referred to in the text, should be numbered sequentially and their identifier enclosed in parenthesis, right justified. The symbols, where referred to in the text, should be italicised.

- point 1
  - point 2
    - point 3

1. numbered point 1
   2. numbered point 2
      3. numbered point 3

$$W(d) = G(A_0, \sigma, d) = \frac{1}{T}\int_0^{+\infty} A_0 \cdot e^{-\frac{d^2}{2\sigma^2}} dt \qquad (1)$$

3 COPYRIGHT

Authors will be asked to sign a copyright transfer form prior to JoMaC publishing of their paper. Reproduction of any part of the publication is not allowed elsewhere without permission from JoMaC whose prior publication must be cited. The understanding is that they have been neither previously published nor submitted concurrently to any other publisher.

4 PEER REVIEW

Papers for publication in JoMaC will first undergo review by anonymous, impartial specialists in the appropriate field. Based on the comments of the referees the Editor will decide on acceptance, revision or rejection. The authors will be provided with copies of the reviewers' remarks to aid in revision and improvement where appropriate.

5 REFERENCES (DESCRIPTION)

The papers in the reference list must be cited in the text. In the text the citation should appear in square brackets [ ], as in, for example, "the red fox has been shown to jump the black cat [3] but not when...". In the Reference list the font should be Times New Roman with 10 point size. Author's first names should be terminated by a 'full stop'. The reference number should be enclosed in brackets.

The book titles should be in *italics*, followed by a 'full stop'. Proceedings or journal titles should be in *italics.* For instance:

REFERENCES (EXAMPLE)

[1] Smith J., Jones A.B. and Brown J., *The title of the book*. 1st edition, Publisher, 2001.

[2] Smith J., Jones A.B. and Brown J., The title of the paper. *Proc. of* C*onference Name*, where it took place, Vol. 1, paper number, pp. 1-11, 2001.

[3] Smith J., Jones A.B. and Brown J., The title of the paper. *Journal Name*, Vol. 1, No. 1, pp. 1-11, 2001.

[4] Smith J., Jones A.B. and Brown J., *Patent title*, U.S. Patent number, 2001.

International Journal of Mechanics and Control – JoMaC
Published by Levrotto&Bella
TRANSFER OF COPYRIGHT AGREEMENT

NOTE: Authors/copyright holders are asked to complete this form signing section A, B or C and mail it to the editor office with the manuscript or as soon afterwards as possible.	*Editor's office address:* Andrea Manuello Bertetto Elvio Bonisoli *Dept. of Mechanics* *Technical University – Politecnico di Torino* *C.so Duca degli Abruzzi, 24 – 10129 Torino – Italy* *e_mail: jomac@polito.it* *fax n.: +39.011.564.6999*

The article title:

By:_____

To be Published in ***International Journal of Mechanics and Control JoMaC***
Official legal Turin court registration Number 5320 (5 May 2000) - reg. Tribunale di Torino N. 5390 del 5 maggio 2000

A Copyright to the above article is hereby transferred to the JoMaC, effective upon acceptance for publication. However the following rights are reserved by the author(s)/copyright holder(s):
1. All proprietary rights other than copyright, such as patent rights;
2. The right to use, free or charge, all or part of this article in future works of their own, such as books and lectures;
3. The right to reproduce the article for their own purposes provided the copies are not offered for sale.

To be signed below by all authors or, if signed by only one author on behalf of all co-authors, the statement A2 below must be signed.

A1. All authors:

SIGNATURE_____DATE_____ SIGNATURE_____DATE_____

PRINTED NAME_____ PRINTED NAME_____

SIGNATURE_____DATE_____ SIGNATURE_____DATE_____

PRINTED NAME_____ PRINTED NAME_____

A2. One author on behalf of all co-authors:
"I represent and warrant that I am authorised to execute this transfer of copyright on behalf of all the authors of the article referred to above"

PRINTED NAME_____

SIGNATURE_____ TITLE_____ DATE_____

B. The above article was written as part of duties as an employee or otherwise as a work made for hire. As an authorised representative of the employer or other proprietor. I hereby transfer copyright to the above article to *International Journal of Mechanics and Control* effective upon publication. However, the following rights are reserved:
1. All proprietary rights other than copyright, such as patent rights;
2. The right to use, free or charge, all or part of this article in future works of their own, such as books and lectures;
3. The right to reproduce the article for their own purposes provided the copies are not offered for sale.

PRINTED NAME_____

SIGNATURE_____ TITLE_____ DATE_____

C. I certify that the above article has been written in the course of employment by the United States Government so that no copyright exists, or by the United Kingdom Government (Crown Copyright), thus there is no transfer of copyright.

PRINTED NAME_____

SIGNATURE_____ TITLE_____ DATE_____

CONTENTS

next number scheduled titles:

Dynamic And Energy Analysis of a Production System of Filament Wound Elbows
G. Dionoro, P. Buonadonna and A. Tronci

Design and Simulation of Cassino Hexapode Walking Machine
G. Carbone, M. Suciu, M. Ceccarelli and D. Pisla

Robot Assisted Laser Scanning
C. Rossi, S. Savino and S. Strano

Evaluation of Feasibility of Mechanical Harvesting of Myrtle Berries (Myrtus Communis L.)
F. Gambella and F. Paschino

Nonlinear Elastic Characteristic of Magnetic Suspensions through Hilbert Transform
E. Bonisoli